submitted to *Geophys. J. Int.*

Imaging laterally-varying regional heterogeneities from seismic coda of single-station records for clustered events

Tae-Kyung Hong and William Menke

Lamont-Doherty Earth Observatory of Columbia University, 61 Route 9W, Palisades, NY 10964, USA.

E-mail: tkhong@ldeo.columbia.edu

SUMMARY

Seismic coda is composed of scattered waves originated from various sources of heterogeneity, some of which might be located well-off the great-circle path between source and receiver. We develop a technique to image laterally-varying regional heterogeneities from seismic coda of single-station records for clustered events. Coherent scattered waves in source-array records are extracted using a slant-stacking. The discrete locations of scatterers are determined by traveltimes, beamforming directions and phase velocities. This technique is applied to regional seismograms of Balapan nuclear explosions, which are recorded at the Borovoye seismic station. The estimated scatterers are correlated with structural variations of surface topography, crustal thickness and sedimentary thickness. The influence of structural variations is investigated by quantifying the scattering strengths in terms of normalized scattering intensity, quality factor and scattering coefficient. The scattering properties vary with phase due to the difference in frequency content and phase velocity. The proposed technique appears to be useful for a study of active tectonic regions with limited monitoring stations.

Key words: Scattering, theory, imaging, attenuation, scattering coefficient, crustal and lithospheric heterogeneity, laterally-varying regional heterogeneity

1 INTRODUCTION

Seismic scattered waves have been rarely used in waveform or traveltime inversion because of the difficulty in identifying their propagation path. Stochastic analyses of scattered waves require no knowledge of propagation paths and have been widely applied, but yield only average estimates of seismic properties of a medium (e.g., Aki & Chouet, 1975; Hoshiba *et al.*, 2001; Lee *et al.*, 2003). Scattered waves that appear before or after teleseismic phases (i.e., precursor or coda) have been used for the study of heterogeneities in the Earth's deep interior (Hedlin *et al.*, 1997; Vidale *et al.*, 1998). The stochastic analysis of seismic attenuation has been found to be useful for qualitative estimation of seismic-hazard potentials in regional areas because seismic attenuation is highly correlated with the seismicity and geology of the region (e.g., Jin & Aki, 1988; Xie & Mitchell, 1990; Tselentis, 1998; Yoshimoto *et al.*, 1998; Chung & Sato, 2001; Wiggins-Grandison & Havskov, 2004). Recently, the complex ray composition of coda has received increasing attention, especially in the context of diffusion theory, which allows us to use the scattered wavefields for seismic imaging (Campillo & Paul, 2003; Snieder, 2004; Shapiro & Campillo, 2004).

In classical stochastic methods, the strength of heterogeneity is quantified in terms of stochastic parameter such as semblance coefficient (e.g., Nikolaev & Troitskiy, 1987; Dainty & Schultz, 1995), scattering coefficient (e.g., Hoshiba *et al.*, 2001) and scattering and intrinsic quality factors (e.g., Aki & Chouet, 1975). Those estimated quantities represent average (stochastic) properties of heterogeneities in the region. Thus, stochastic methods require dense seismic recording to resolve the properties of discrete (localized) heterogeneity. In those methods, the volume of study area is discretized into a set of 3-D cells, and the scattering quantities are estimated for each cell (Chen & Long, 2000; Taira & Yomogida, 2004). Another method to study discrete heterogeneities is to migrate diffracted waves from a teleseismic phase (Revenaugh, 1995, 2000). The method calcuates the position of heterogeneity by analyzing the arrival-time differences across receiver array. This migration method requires array recording to image heterogeneities beneath stations.

Dense networks of stations are required for conventional methods. However, inaccessible areas (e.g., oceanic environment) or aseismic areas do not allow such dense seismic recording. Teleseismic-wave tomography can be used for such environments, but crustal

structures are still difficult to resolve, owing to the long wavelength of teleseismic waves. In this study, we propose a technique to image laterally-varying regional heterogeneities using single-station records of clustered events. Coherent scattered waves are collected with a slant-stacking of source-array records. We use crustal and mantle-lid scattered waves and constrain the depth of imaging. A double-beamforming technique, in which both source and receiver arrays are used, would allow -in principle- precise positioning of scatterer. Double-beamforming has been successfully applied in a teleseismic context, to image heterogeneities in the earth's deep interior (Scherbaum *et al.*, 1997; Krüger *et al.*, 2001). Cases in which both source and receiver array are available are rare unfortunately. We concentrate here on what can be learned from a single, source-side array.

In the course of this study, we investigate the nature of coda, and discuss a way to quantify the scattered energy from the coda. We characterize the scattering features with respect to structural variations (crustal thickness, sedimentary thickness, surface topography). We present a technique to measure the scattering properties of individual heterogeneity in terms of quality factor and scattering coefficient.

2 THEORY

2.1 Energy partition of regional waves by scattering

During scattering, body waves experience wavetype-coupling (*S*-wave excitation by *P*-wave scattering, and vise versa) and surface waves incorporate mode-coupling (higher-mode surface-wave excitation by fundamental-mode surface-wave scattering, and vice versa). This coupling process causes partition in incident energy.

The energy partition by wavetype-coupling during scattering is well understood (Frankel & Clayton, 1986; Hong & Kennett, 2003; Hong, 2004). We investigate the energy partitioning by wavetype-coupling for an elastic medium with seismic properties typical of continental crust: α=5.8 km/s and β=3.46 km/s. Compressional velocity, α, and shear velocity, β, and density, ρ, are correlated so that their perturbations $\delta\rho$, $\delta\beta$ and $\delta\rho$ obey the empirical relationship (Shiomi *et al.*, 1997):

$$\xi(\mathbf{x}) = \frac{\delta\alpha(\mathbf{x})}{\alpha_0} = \frac{\delta\beta(\mathbf{x})}{\beta_0} = \frac{1}{K}\frac{\delta\rho(\mathbf{x})}{\rho_0}, \tag{1}$$

where $\xi(\mathbf{x})$ is the normalized velocity perturbation at a location of $\mathbf{x}$, and K is a constant to control the strength of density perturbation relative to the velocity perturbation. The parameters α_0 and β_0 are the background compressional and shear velocities, and ρ_0 is the background density. We set K to be 0.8 (Sato & Fehler, 1998).

We examine the energy partition at three different random media (Gaussian, exponential, von Karman) (e.g., Hong & Kennett, 2003). The theoretical partitioning of scattered energy is given in Hong & Kennett (2003) and Hong (2004) (also see, Appendix A). Fig. 1 shows the variation of energy ratio between in-phase and wavetype-coupled scattered waves as a function of normalized wavenumber, ka. The energy ratio is calculated by

$$R = \frac{\int_\phi \langle |u^c(\phi)|^2 \rangle d\phi}{\int_\phi \langle |u^i(\phi)|^2 \rangle d\phi}, \tag{2}$$

where ϕ is the scattering angle, $\langle |u^i(\phi)|^2 \rangle$ is the ensemble-averaged amplitude square of in-phase scattered wave, and $\langle |u^c(\phi)|^2 \rangle$ is for coupling-phase scattered wave. The ensemble-averaged amplitudes in (2) are given in Appendix A.

For shear-wave incidence, the energy ratio (R) is lower than 0.04 for the entire ka range. This indicates that in-phase scattering is the dominant scattering mechanism for shear waves at any frequencies and heterogeneity scales. This theoretical expectation agrees with the field observation that local *S* coda is dominantly composed of shear scattered waves (e.g., Aki, 1980; Fehler *et al.*, 1992). In contrast, for compressional-wave incidence, wavetype-coupled scattered waves are dominant over the in-phase scattered wave at low ka ($ka < 1$). The in-phase scattering is strong at high ka ($ka > 1$). This observation indicates that wavetype coupling process is strong in scattering of low-frequency *P* waves. For instance, when a *P* wave with a dominant frequency of 2 Hz propagates through a heterogeneous medium with a correlation distance of 9 km or smaller, the scattered wavefield will be mainly composed of scattered shear waves.

The resolving power of array analysis depends on the array aperture, array configuration and interstation spacing (interevent spacing for source array system). Scatterers that are not sufficiently larger than the interstation interval are not resolved well in a large aperture array system, because the waves scattered from small heterogeneities do not produce coherent phases resolvable by the array. Moreover, scattering strength is peak around $ka = 1$ and declines exponentially with decreasing ka (Frankel & Clayton, 1986; Hong & Kennett, 2003). Thus, the influence of the wavetype-coupled shear scattered waves from small-scale heterogeneity is negligible compared to those from large-scale heterogeneity such as geological variations.

A mode coupling is expected in surface-wave scattering, and the radiation patterns of mode-coupled scattered waves are well understood (e.g., Snieder, 1986; Bostock, 1991). The radiation pattern changes with the coupled mode, but there is a stochastic equivalence between lost and earned energy during the mode couplings (Snieder, 1988). Thus, the

stochastic energy partition by mode coupling during scattering can be regarded as an isotropic scattering process (Snieder, 1988; Sato & Nishino, 2002). We see that the scattered wavefields from regional waves can be well explained with an in-phase scattering process. Thus, under single in-phase concept, we can estimate the scatterer locations with the incident direction, traveltime and phase velocity of coherent scattered wave (Fig. 2).

2.2 Extraction of coherent scattered energy

We use single-station records for clustered events (source-array records) in this study. Analyses of such source-array records have been applied well for the investigation of wavefield and physical properties of source region (Spudich & Bostwick, 1987; Gupta *et al.*, 1990; Scherbaum *et al.*, 1991; Xie *et al.*, 1996; Hong & Xie, 2005). We extract coherent scattered energy from source-array records using a slant-stacking (Kanasewich, 1981; Matsumoto *et al.*, 1998; Rost & Thomas, 2002). The beamforming is made for all azimuthal directions ($0 \leq \theta < 2\pi$). Multi-scattered and incoherent scattered waves are suppressed during the slant-stacking. Multi-scattered waves, which may be included in the stacked record, are typically weaker than the single-scattered waves with the same phase velocity due to geometrical spreading and multiple energy-partitioning during multiple scattering.

The slant-stacked record, $u_s^j(t)$, of source-array records for a beamforming direction of θ_j can be calculated by

$$u_s^j(t) = \frac{1}{M}\sum_{i=1}^{M} u_i(t - \Delta r_i^j \cdot s_h), \tag{3}$$

where u_i is the seismogram for the ith event, M is the number of total events, and s_h is the horizontal slowness. Δr_i^j is given by

$$\Delta r_i^j = r_i^j - r_0, \tag{4}$$

where r_i^j is the distance between an event location of $\mathbf{x}_i$, and an imaginary location of $\mathbf{y}_j$, which is placed in an beamforming direction of θ_j. The reference radius, r_0, is the distance between the station and sources (Fig. 3). The reference location, $\mathbf{y}_j$, can be calculated by

$$\mathbf{y}_j = \mathbf{x}_0 + (r_0 \sin\theta_j, r_0 \cos\theta_j), \tag{5}$$

where $\mathbf{x}_0$ is the reference location of the sources, which corresponds to the center of the events. Here, r_0 should be sufficiently larger than both Δr_i^j and array aperture, L_{ap} (i.e., $r_0 \gg \Delta r_i^j$, $r_0 \gg L_{ap}$) to satisfy the plane-wave approximation for array analysis. Fig. 4 shows an example of slant-stackings for two different beamforming directions. The apparent

distance, r_i^j, changes with beamforming direction, θ_j. Thus, the order of records as function of distance changes with θ_j.

It is noteworthy that the natures of extracted waves are different between receiver- and source-array systems. The phase velocity estimated from receiver-array data corresponds to the phase velocity of wave after scattering. On the other hand, the phase velocity from source-array data indicates the phase velocity of wave before scattering. Thus, the identity of incident wave to scatterer is unknown under receiver array system. In a source array analysis, the incident phase and its incident direction are known. Since we know both the traveltime of the extracted scattered wavelet and its initial phase velocity, we can determine the location of scatterer under the single in-phase scattering theory (Fig. 2).

3 DATA AND GEOLOGY

We use seismic records of the Borovoye station (BRV) for underground nuclear explosions (UNE) at the Balapan test site, Kazakhstan of a time period between 1968 and 1989. The body-wave magnitudes, m_b, of UNE range between 4.8 and 6.2. The distances between BRV and UNE are around 690 km (Fig. 5). High-precision UNE locations and origin times are available from various sources (NNCRK, 1999; Thurber *et al.*, 2001; Kim *et al.*, 2001).

The recording system of BRV is composed of a set of short-period displacement instruments (Kim *et al.*, 2001; Hong & Xie, 2005). The sensor type of the seismometers is SKM-3 with a natural period of 2.0 s and sampling rates of 0.032 and 0.096 s. The nominal sensitivities (gains) of the seismometers are 20, 200, 1000 and 2000 counts/μm (Kim *et al.*, 2001). Since coda waves attenuate exponentially with time, we use both low-gain (20, 200 counts/μm) and high-gain (1000, 2000 counts/μm) seismograms in this study to avoid digital round-off error, switching from low-gain to high-gain after a lapse time of 400 s. The numbers of low- and high-gain records are 46 and 35, respectively (Fig. 5). The records display a high signal-to-noise ratio (S/N> 50 dB) (Fig. 5).

The southwestern area of the Balapan test site is covered with crystalline rocks, and the northeastern area is on alluvium (Ringdal *et al.*, 1992). This difference in surface geology causes a crustal shear velocity difference between the areas by about 0.4 km/s (Bonner *et al.*, 2001). In this study, we analyze records for UNEs detonated at the southwestern region where most Balapan UNEs are clustered (Fig. 6). The aperture of the source array is around 19 km in the longitudinal direction (Fig. 6(b)). The average depth of burial is 465 m below the

surface, and the average depth deviation is 73 m. The average horizontal spacing between adjacent events is 1.42 km.

The compressional and shear velocities in the crust of Kazakhstan increase with depth, and reach 8.0 and 4.7 km/s at the mantle lid (Quin & Thurber, 1992). The crustal thickness (CRUST2.0, Bassin *et al.* (2000)), sedimentary layer thickness (Laske & Masters, 1997), surface topography (GTOPO30, compiled by the U.S. Geological Survey), and major geological setting (e.g., Levashova *et al.*, 2003) are shown in Fig. 7. Thick sedimentary layers (Fig. 7(b)) correspond to geological basins and cratons (Fig. 7(d)); A is the West Siberian Basin, B the European Craton, C the Tarim Basin, and E is the Turan plate. The hard rock area, D, in which the Balapan test site and the Borovoye Observatory are placed is composed of precambrian and early palaeozoic rocks (Levashova *et al.*, 2003).

4 SOURCE-ARRAY CONFIGURATION AND CONDITIONS

The aperture of source array, L_{ap}, is about 19 km, the average interval between adjacent events, l_a), is 1.42 km, and the average depth deviation, Δd, is 73 m. The depth deviation is fairly small relative to the interevent distance, $\Delta d/l_a = 0.051$. Thus, we can assume that the source-array components are placed on a horizontal plane. However, erroneous estimation of phase velocity can be made due to apparent phase shift by vertical variation of array components. The condition to neglect the influence of vertical variation of array components is that the wavelength of analyzed phase is sufficiently larger than the vertical dimension of array (Spudich & Bostwick, 1987):

$$\lambda_p > 4\Delta d, \tag{6}$$

which is equivalent to

$$f_p < \frac{v}{4\Delta d}, \tag{7}$$

where λ_p is the wavelength of phase, f_p is frequency of phase, v is the phase velocity, and Δd is the vertical standard deviation of event locations.

Surface waves, *Rg*, have the shortest wavelength in this study. They, together with the station spacing, imply that spatial aliasing occurs above 8.5 Hz, thus placing an upper limit on the frequencies that can be analyzed. This critical frequency is larger than the nyquist frequency of data set, 5.2 Hz. We analyze frequencies only up to 3.0 Hz in this study. Therefore, the aliasing effect by vertical variation of array components can be neglected in the array analysis. We additionally examine the response functions of the source array for the

frequency bands which are used in the study (Rost & Thomas, 2002). The slowness power spectrum energies are concentrated in the centers of the diagrams, which indicates a high resolution of array analysis for the given frequency bands (Fig. 8).

5 SCATTERED WAVE: COHERENCE AND DIFFUSION

Seismic coda is composed of complex scattered waves bearing various ray-path trajectories. When multiple scattering dominates, the wavefield is diffusive and stochastic properties of the wavefield are spatially uniform. In this case, the Green function of medium can be estimated from cross-correlations of seismic records between pairs of stations (Campillo & Paul, 2003; Snieder, 2004; Shapiro & Campillo, 2004).

We examine the phase composition and incoming direction of scattered energy in coda. We apply a frequency-wavenumber (F-K) method to bandpass filtered coda of the source-array records. The bandpass filtering ranges are 0.2 to 0.4 Hz, 0.4 to 0.8 Hz, 0.8 to 1.6 Hz, and 1.6 to 3.2 Hz. We observe strong and coherent scattered energy with a phase velocity of 3.0 km/s in the slowness power spectra at a frequency band of 0.2 to 0.8 Hz (Fig. 9(a),(b)). The phase velocity corresponds to the *Rg* phase velocity (Hong & Xie, 2005). This dominant phase is observed consistently until the end of records, 900 s after the origin times, which corresponds to about 4 times of the *Rg* traveltime.

Scattered waves at high frequencies, above 0.8 Hz, appear to be diffusive (Fig. 9(c),(d)) (e.g., Del Pezzo *et al.*, 1997). This is because high frequency waves are strongly influenced by small-scale heterogeneities that are widely distributed in the crust and mantle-lid due to their small mean free paths (correlation distances). On the other hand, large-scale heterogeneities appear to be less effective for the construction of diffuse wavefield. Thus, the diffusion approximation for coda analysis (Shapiro *et al.*, 2000; Campillo & Paul, 2003) appears to be valid to high-frequency scattered waves ($f > 0.8$ Hz). Considering the frequency content, hereafter, we analyze *Rg* scattered waves in a frequency range of 0.2 to 0.8 Hz, *Lg* scattered waves in a frequency range of 0.5 to 2.5 Hz, and *Sn* and *Pg* in 0.5 to 3.0 Hz.

6 ISOCHRONOUS SCATTERING POWER

We observe coherent scattered waves throughout the coda (see, Section 5). The coherent scattered energy is estimated from slant-stacked records. The horizontal slownesses (phase velocities) of major phases in the regional records are used for the slant-stackings. The phase velocities of major regional phases of source-array records are determined by

frequency-wavenumber analyses. The estimated phase velocities of *Rg*, *Lg*, *Sn* and *Pg* are 3.0, 4.2, 4.8 and 7.1 km/s, respectively (Hong & Xie, 2005). These estimates of phase velocities agree with the seismic structure of Kazakhstan (Der *et al.*, 1984; Quin & Thurber, 1992).

The scattering intensity is proportional to the fractional energy loss ($\Delta E/E$). The scattered energy can be estimated with average amplitude squares, w_s^{θ}, of coherent scattered waves in a given time window:

$$w_s^{\theta_j}(t_n) = \frac{1}{N}\sum_{k=1}^{N}\left|u_s^j(t_{n-N/2+k})\right|^2, \tag{8}$$

where θ_j is the jth azimuthal angle (beamforming direction), t_n is the nth discrete time, u_s^j is the slant-stacked record for an azimuthal angle of θ_j in equation (3), and N is the total number of discrete times in time window.

The bandpass filtering range and time-window size for slant-stacking are adjusted considering the frequency content of phase. The bandpass filtering ranges are 0.2 to 0.8 Hz for *Rg* phase, 0.5 to 2.5 Hz for *Lg*, and 0.5 to 3.0 Hz for *Sn* and *Pg*. We use a 30-s window for *Rg*, 20-s window for *Lg*, and 14-s window for *Sn* and *Pg* phases. The analysis is performed from the arrival time of phase to a lapse time of 900 s. Low-gain records are used by a lapse time of 400 s, and high-gain records are applied for the later times. Normalized scattering intensity, P_s , is estimated by

$$P_s(\theta_j, t_n) = \frac{w_s^{\theta_j}(t_n)}{w_{\max}(t_n)}, \tag{9}$$

where $w_{\max}(t_n)$ is the maximum scattering intensity of isochrone

$$w_{\max}(t_n) = \max\left[w_s^{\theta_j}(t = t_n),\ j = 1, 2, \ldots, J\right], \tag{10}$$

and J is the number of discrete azimuthal angles. In Fig. 10, we present *Rg* scattering intensities for several lapse times. The integrated results for all lapse times are shown in Fig. 11. The times annotated in the figure are the lapse times, and the angles are the beamforming directions. The temporal variation of scattering intensity can be inverted for a spatial distribution of scatterers under the single in-phase scattering approximation (Fig. 12).

We test the single in-phase scattering concept by comparing the spatial variation of scattering intensity with that of a scheme allowing a wavetype coupling. In Fig. 13, we present the spatial variation of scattering intensity under assumption that incident *Lg* wave is dominantly scattered into *Pg* phase. The isochrone, that has two foci at source and station locations but with a higher phase velocity for scattered waves, appears as an oval with a symmetric axis along the great-circle path. The mapped locations of heterogeneities appear

to be less well-correlated with the known geological variations than those made using the in-phase scattering concept (Fig. 12(b)). For instance, the spatial variation of scattering intensity is not correlated with high topography area around 45°N and 82°E. This result confirms the in-phase scattering theory is a reasonable approximation for mapping regional heterogeneities.

The overall features of scattering intensity appears to be consistent among various phases (Fig. 12). The illuminated locations of scatterers agree with the structural variations in the crust and lithosphere (e.g., Zhang & Lay, 1994; Dainty & Schultz, 1995; La Rocca *et al.*, 2001). However, scatterer locations inferred from different seismic phases are somewhat different due to the difference in ray paths and frequency contents. *Lg* wave is a set of crustally-guided shear waves which typically have group velocities of 3.0 to 3.6 km/s (e.g., Kennett, 2002). This *Lg* wave is also regarded as a higher-mode Rayleigh wave in a mode theory, while *Rg* is the fundamental mode of Rayleigh wave. Both *Rg* and *Lg* present similar features in the imaging. However, *Rg* decreases exponentially decreases with depth and *Lg* has a higher phase velocity than *Rg*. Thus, *Lg* appears to be much practical for imaging of lower crust, while *Lg* is less sensitive to the surface topography.

The scatterer locations illuminated from *Sn* phase are close to those from *Lg* phase, but the crustal thickness is reflected slightly better in the *Sn* result. The scattering of *Pg* phase is strong at most structural variations. Since *Pg* phase has a greater wavelength and higher frequency content than surface waves (*Rg*, *Lg*), the *Pg* is more sensitive to the gradient of structural variation, e.g., regions with high gradients of crustal-thickness variation, around 67°E & 54°N, and 65°E & 57°N.

7 Q

We estimate the strengths of heterogeneities in terms of apparent quality factors. The temporal decay of coda can be represented with a simple equation (Toksöz *et al.*, 1988; Sato & Fehler, 1998):

$$A(t) = A_0 \frac{1}{t^p} \exp\left[-\frac{\omega t}{2Q_c}\right], \tag{11}$$

where ω is the angular frequency, t is a lapse time, A_0 is a constant for the initial level of coda, and p is the geometrical spreading parameter $p = 1.0$ for body waves, $p = 0.75$ for diffuse waves, and 0.5 for surface waves. We analyze late coda at lapse times after 500 s where multiple scattered waves are well mixed. The lapse time of 500 s corresponds to 4.5 times of *Pg* traveltime, 3 times of *Sn* traveltime, 2.5 times of *Lg* traveltime, and twice of

Rg traveltime. We estimate average Q_c from the source-array codas. The scattered waves with surface phase velocities are dominant in coda at low frequencies, and the composition of body waves increases with frequency (Section 5). *Rg* phase is observed dominantly in a frequency band of 0.2 to 0.8 Hz, and *Lg* phase is observed consistently up to a frequency of 2.0 Hz in regional coda. In contrast, body waves are observed in all frequency ranges, and are relatively much strong at high frequencies (Hong & Xie, 2005). We apply 0.5 to p for records with a low pass filter lower than 2.0 Hz, and 1.0 for those of higher frequencies. The mean quality factors are measured by 1201 ± 66 for the records of 0.5-3.0 Hz, 742 ± 36 for the records of 0.5-2.0 Hz, and 361 ± 29 for the records of 0.2-0.8 Hz.

Under the first-order Born scattering theory where scattered energy, ΔE, is assumed to be far less than the incident energy, E_0 (i.e., $\Delta E \ll E_0$), the amplitude of wavefront is constant over an isochrone (Aki & Richards, 1980). With an assumption of single isotropic scattering, the total scattered energy from a heterogeneity on an isochrone is given by

$$\Delta E(\theta, t) = 4\pi E_s(\theta, t), \tag{12}$$

where $E_s(\theta, t)$ is the scattered energy of a slant-stacked record with a beamforming direction of θ and a lapse time of t. The total scattered energy on an isochrone with a traveltime of t is given by

$$\Delta E_T(t) = \int_0^{2\pi} \Delta E(\theta, t)\, \delta\theta. \tag{13}$$

Thus, the average angular scattered energy is then given by

$$\langle \Delta E \rangle(t) = \frac{1}{2\pi} \Delta E_T(t) = \frac{1}{J} \sum_{j=1}^{J} \Delta E(\theta_j, t), \tag{14}$$

where J is the number of discrete azimuthal angles, and $\langle \Delta E \rangle(t)$ is the average scattered energy level at a lapse time of t.

The scattered energy is proportional to the square of amplitude of scattered wave. The coda of single-station record shares the same temporal decay rate with that of slant-stacked record, but with different energy levels (Matsumoto *et al.*, 2001). Thus, the Q_c estimated from source-array records can be applied for an analysis of slant-stacked records. From (11), the square of coda amplitude ($w(t)$) is given by

$$w(t) = w_0 \frac{1}{t^{2p}} \exp\left[-\frac{\omega t}{Q_c}\right], \tag{15}$$

where w_0 is a constant. From equation (15), every slant-stacked coda can be represented by

$$w_s^{\theta}(t) = w_0^{\theta} \frac{1}{t^{2p}} \exp\left[-\frac{\omega t}{Q_c}\right], \tag{16}$$

where $w_s^\theta(t)$ is the square of amplitude of slant-stacked coda with a beamforming direction of θ, and w_0^θ varies with the beamforming direction of slant-stacking.

The seismic quality factor is inversely proportional to the energy loss (Aki & Richards, 1980; Wu, 1982):

$$Q^{-1}(k) = \frac{1}{Vk}\frac{\Delta E}{E}, \tag{17}$$

where k is the wavenumber, and V is the volume of heterogeneous medium which incident wave passes through. Coda level of a record can be temporally increased due to inhomogeneous distribution (localization) of heterogeneities in medium. Similarly, a reference quality factor, Q_{ref}, can be expressed with known dissipated energy, ΔE_{ref}, by:

$$Q_{ref}^{-1}(k) = \frac{1}{Vk}\frac{\Delta E_{ref}}{E}, \tag{18}$$

From equations (17) and (18), the ratio of quality factors can be written by:

$$\frac{Q}{Q_{ref}} = \frac{\Delta E_{ref}}{\Delta E}. \tag{19}$$

The attenuated energy by scattering, ΔE, is proportional to the amplitude square of scattered wave, w_s^θ in equation (16). Thus, we can measure temporal quality factor, $Q(\theta, t)$, of a slant-stacked coda by

$$Q(\theta, t) = Q_{\mathrm{ref}}\left[\frac{w_{\mathrm{ref}}^\theta(t)}{w_s^\theta(t)}\right], \tag{20}$$

where Q_{ref} is a reference Q, and $w_{\mathrm{ref}}^\theta(t)$ is a reference level of coda estimated from equation (16).

The temporal decay of coda is not well-represented with a deterministic value of A_0 due to the temporal change in coda composition, from single-scattered waves early in the coda to multiply-scattered waves late in the coda (Lee & Sato, 2005; Jemberie and Langston, 2005). We divide the record sections into several segments to examine these changes. The record sections are segmented into 310-340 s, 340-400 s, and 400-900 s for an analysis of *Rg* scattered energy, 270-300 s, 300-340 s, 340-400 s and 400-900 s for *Lg* scattered energy, 210-240 s, 240-280 s, 280-330 s, 330-400 s and 400-900 s for *Sn* scattered energy. For *Pg* scattered energy, we use time segmentations of 160-190 s, 190-230 s, 230-280 s, 280-340 s, 340-400 s and 400-900 s.

The apparent quality factors projected on a map are shown in Fig. 14. The Q estimates agree with a previous Q model of Jin & Aki (1988). The Q values from *Rg* and *Lg* scattered waves are lower than those from *Sn* and *Pg* scattered waves. This Q feature agrees with a frequency power law (e.g., Mitchell, 1981; Dahlen & Tromp, 1998, pp.216):

$$Q(f) = Q_0 f^\eta, \tag{21}$$

where f is a frequency, Q_0 is the quality factor at 1 Hz, and η is the frequency dependence factor which is given around between 0.2 and 1.8 (e.g., Campillo *et al.*, 1985; Cheng & Kennett, 2002; Vargas *et al.*, 2004; Padhy, 2005).

Rg wave is scattered strongly for all large-scale heterogeneities in the crust. The quality factor is $Q_{Rg} \approx 400$, except for regions of crustal thinning, where it is lower ($Q_{Rg} \approx 100$). This crustal thinning, which has an amplitude of about 10 km (Bassin et al., 2000), appears to be a primary source of *Rg* attenuation. *Lg* wave is also sensitive to large-scale variations in the crust, and particulary to the variation of sedimentary thickness. The quality factor is measured by around 400 at a place with a sedimentary thickness change of 7 km. *Lg* waves are strongly disrupted by crustal thinning, while only weakly influenced by crustal thickening (Kennett, 1986). *Lg* has quality factors of $Q_{Lg} = 320$ for a 10-km crustal thinning, and $Q_{Lg} = 420$ for a 10-km crustal thickening. The *Lg* waves attenuate less for a surface topography variation compared to *Rg*, and have $Q_{Lg} = 550$ in regions with 2 km of relief.

The *Sn* phase is strongly sensitive to variations of crustal thickness and sediment thickness, but only weakly sensitive to the surface topography. The quality factor is estimated to be $Q_{Sn} = 400$ for region of 10-km crustal thinning and 650 for a region of sedimentary-thickness change of 7 km. The *Pg* phase appears to be sensitive to a variation of crustal thickness, but weakly influenced by a variation of sedimentary thickness and a mild surface topography ($\Delta h < 3$ km). However, an abrupt large-scale variation of surface topography ($\Delta h > 4$ km) causes a strong scattering (e.g., Q at the Tarim Basin). The quality factor is given by $Q_{Pg} = 320$ for a crustal-thickness variation of 10 km, and 700 for a surface-topography change of 4 km. From the observed Q, each phase appears to behave differently to crustal and lithospheric structures. This observation agrees with Zhang & Lay (1994) in which the energy loss by a surface-topography change varies with phase. This difference is associated with the phase velocity that confines the depth of imaging.

8 SCATTERING COEFFICIENT

The scattering coefficient quantifies the strength of heterogeneity. The scattering coefficient (turbidity coefficient), g, is defined as the fractional energy loss per unit propagation distance (Chernov, 1960):

$$g = \frac{\Delta E}{EL}, \tag{22}$$

where ΔE is the energy loss by scattering, E the incident energy, and L the propagation distance. The representative scattering coefficient (namely, "total scattering coefficient", g_0),

is defined as the average over all scattering directions (i.e., solid angle, 4π) (Sato & Fehler, 1998):

$$g_0 = \frac{1}{4\pi} \int_{\psi} \int_{\phi} g(\psi, \phi)\, d\psi\, d\phi = \frac{k}{Q_s}, \tag{23}$$

where k is the wavenumber of incident wave, and Q_s is the scattering attenuation factor. Thus, when the scatterers are isotropic heterogeneities, $g(\theta, \psi)$ is equal to g_0 in every direction (Herraiz & Espinosa, 1987; Sato & Fehler, 1998). The inverse of the scattering coefficient, $1/g_0$, is referred as the mean free path, l.

From equation (23), the scattering attenuation factor can be written by (e.g., Dainty, 1981)

$$Q_s^{-1} = \frac{g_0 v}{\omega}, \tag{24}$$

where v is the phase velocity, and ω is the angular frequency of incident wave. The observed seismic attenuation is a result of combined influence of intrinsic and scattering attenuations (Q_i, Q_s):

$$\frac{1}{Q_t} = \frac{1}{Q_i} + \frac{1}{Q_s}. \tag{25}$$

From (24) and (25), the scattering coefficient, g_0, can be estimated with a given Q_i:

$$g_0 = \frac{\omega}{v} \left(\frac{1}{Q_t} - \frac{1}{Q_i} \right), \tag{26}$$

where Q_t is determined in Section 7.

The separation of intrinsic and scattering attenuations has been widely adopted in the coda-envelope analyses of local seismograms (e.g., Hoshiba, 1993; Pujades *et al.*, 1997). The scattered waves recorded in local seismograms are mainly originated from near-surface heterogeneities, which are regarded to be distributed in an one-layer medium. Thus, the determined scattering and intrinsic attenuation represents the stochastic properties of local heterogeneities. On the other hand, the coda of regional seismograms contains both regional scattered waves and deep seismic phases (Lee *et al.*, 2003). Thus, the analysis of envelope analysis of regional coda requires that the seismic structures of the Earth should be taken into account, and needs a regional network for stochastic estimation (Yoshimoto, 2000; Lee *et al.*, 2003). However, this study is based on a single-station records of clustered events, which hold one principle great-circle direction. Thus, we can only determine intrinsic quality factors approximately from late coda, in which diffused multi-scattered waves are dominant. The temporal attenuation of the late coda is mainly controlled by inelastic-absorption processes (e.g., Shapiro *et al.*, 2000; Margerin, 2005). In this case, the Q_c of late coda is equivalent to the intrinsic Q. This relationship can be derived also from the envelope expression based on energy-flux model (Frankel & Wennerberg, 1987). The intrinsic quality factors are

determined from codas at lapse times of 750 to 900 s. We obtain intrinsic quality factors by 537 ± 17 with records of 0.2-0.8 H, 1075 ± 34 with records of 0.5-2.0 Hz, and 1526 ± 49 with records of 0.5-3.0 Hz. The study area is a tectonically stable region which is mostly composed of areas with a precambrian-palaeozoic basement. The estimated intrinsic quality factors agree with other studies on stable regions with hard-rock basements (Campillo & Plantet, 1991; Pujades *et al.*, 1997).

We now calculate the scattering coefficient from equation (26) (Fig.15). The spatial variation of scattering coefficients appears to follow the Q pattern in Section 7. The estimated scattering coefficients agree with the observations from other tectonically-stable regions (Padhy, 2005). The apparent scattering coefficient estimated from *Rg* scattered waves is given by $g_0 \approx 0.006$ km^{-1} in a region with a crustal thinning of 10 km. A significant *Rg* scattering is caused by the presence of a sedimentary basin due to the blockage of lateral waveguide, and scattering coefficient is estimated by $g_0 \approx 0.01$ km^{-1} in a region with 4-km sedimentary thickening. The scattering coefficient is estimated as $g_0 \approx 0.003$ km^{-1} for a surface-topography change of 2 km. The overall scattering coefficients estimated from *Lg* scattered waves are smaller than those from *Rg* scattered waves. The scattering coefficients from *Lg* scattered waves are given by 0.004 km^{-1} for a crustal thickening of 10 km, 0.006 km^{-1} for a crustal thinning of 10 km, and 0.003 km^{-1} for 4-km sedimentary thickening. Scattering coefficient for a surface-topography change of 2 km is given by 0.002 km^{-1}.

The magnitudes of *Sn* scattering coefficients are estimated by about a half of the *Lg* scattering coefficients, but their spatial variations appear to be close. In particular, *Sn* phase is strongly scattered by the sedimentary blockage at a location of 49°N and 54°E, and the scattering coefficient reaches to 0.0045 km^{-1}, which is a comparable magnitude to that of *Lg* scattering coefficient. The magnitudes of *Sn* scattering coefficients are smaller than 0.0015 km^{-1}, except areas in which large gradients of changes in crustal thickness are observed. The *Sn* scattering coefficient is estimated by around 0.003 km^{-1} for a crustal thickening of 10 km. It appears that both surface topography and sedimentary blockage contribute less to *Pg* scattering than crustal-thickness variation. Overall, we find that the scattering coefficient varies with phase. This is because the depth of imaging changes with the phase velocity and the scattering magnitude is dependent on the frequency.

9 DISCUSSION AND CONCLUSIONS

We have devised a technique using source-array records to image laterally-varying regional heterogeneities. The estimated scattering intensity illuminates large-scale structural

variation which is associated with crustal thickening/thinning, sedimentary blockage and surface topography. The apparent attenuation factors and scattering coefficients vary with both phase velocity and frequency. The influence of various types of geological heterogeneity varies significantly between wave type.

The proposed technique shows promises for studying laterally-varying geological and tectonic structures of a region where limited seismic monitoring is available (e.g., low great-circle path coverage, limited number of available stations). Such regions include subduction zones and mid-ocean ridges where clustered events are naturally placed. The technique is able to detect topographic variation of internal boundaries within the crust and lithosphere. Thus, the technique can be extended for sounding of intrusive or high-impedance materials, such as magma chamber and partial melting material (Tusa *et al.*, 2004).

In this study, we have used regional seismograms for nuclear explosions which have high-precision information of locations and origin times. When one applies the technique presented in this study to natural earthquakes, it may be required to refine the locations and origin times using waveform cross-correlation techniques (e.g., VanDecar & Crosson, 1990; Waldhauser & Ellsworth, 2000).

ACKNOWLEDGMENTS

We thank Jiakang Xie for valuable discussions on the F-K analysis for source array data. We are grateful to Won-Young Kim, Vitaly Khalturin, and Paul Richards for information on Balapan explosion data. TKH is grateful to Won Sang Lee for discussion on Q in central Asia. We thank Prof. Michael Korn and two anonymous reviewers for fruitful comments. The work was partially supported by DOE grant, DE-FC52-03NA99514. This is Lamont-Doherty Earth Observatory contribution XXXX.

REFERENCES

Aki, K., 1980. Attenuation of shear-waves in the lithosphere for frequencies from 0.005 to 25 Hz, *Phys. Earth Planet. Inter.*, **21**, 50-60.

Aki, K. & Chouet, B., 1975. Origin of coda waves: Source, attenuation, and scattering effects, *J. Geophys. Res.*, **80**, 3322-3342.

Aki, K. & Richards, P.G., 1980. *Quantitative Seismology, Theory and Methods*, volume II, W.H. Freeman and Company, San Francisco.

Bassin, C., Laske, G., & Masters, G., 2000. The current limits of resolution for surface wave tomography in North America, *EOS Trans AGU*, **81**, F897.

Bonner, J.L., Pearson, D.C., Phillips, W.S., & Taylor, S.R., 2001. Shallow velocity structure at the Shagan River test site in Kazakhstan, *Pure Appl. Geophys.*, **158**, 2017-2039.

Bostock, M.G., 1991. Surface wave scattering from 3-D obstacles, *Geophys. J. Int.*, **104**, 351-370.

Campillo, M. & Paul, A., 2003. Long-range correlations in the diffuse seismic coda, *Science*, **299**, 547-549.

Campillo, M. & Plantet, J.L., 1991. Frequency dependence and spatial distribution of seismic attenuation in France: experimental results and possible interpretations, *Phys. Earth Planet. Inter.*, **67**, 48-64.

Campillo, M., Plantet, J.L., & Bouchon, M., 1985. Frequency-dependent attenuation in the crust beneath central France from *Lg* waves: Data analysis and numerical modeling, *Bull. Seism. Soc. Am.*, **75**, 1395-1411.

Chen, X. & Long, L.T., 2000. Spatial distribution of relative scattering coefficients determined from microearthquake coda, *Bull. Seism. Soc. Am.*, **90** (2), 512-524.

Cheng, H.-X. & Kennett, B.L.N., 2002. Frequency dependence of seismic wave attenuation in the upper mantle beneath the Australian region, *Geophys. J. Int.*, **150**, 45-57.

Chernov, L.A., 1960. *Wave Propagation in a Random Medium*, McGraw-Hill, New York.

Chung, T.-W. & Sato, H., 2001. Attenuation of high-frequency *P* and *S* waves in the crust of southeastern South Korea, *Bull. seism. Soc. Am.*, **91**, 1867-1874.

Dahlen, F.A. & Tromp, J., 1998. *Theoretical Global Seismology*, Princeton University Press, New Jersey, p.1025.

Dainty, A.M., 1981. A scattering model to explain seismic *Q* observations in the lithosphere between 1 and 30 Hz, *Geophys. Res. Lett.*, **8**, 1126-1128.

Dainty, A.M. & Schultz, C.A., 1995. Crustal reflections and the nature of regional *P* coda, *Bull. Seism. Soc. Am.*, **85**, 851-858.

Del Pezzo, E., La Rocca, M., & Ibanez, J., 1997. Observations of high-frequency scattered waves using dense arrays at Teide Volcano, *Bull. Seism. Soc. Am.*, **87**, 1637-1647.

Der, Z.A., Marshall, M.E., O'Donnell, A., & McElfresh, T.W., 1984. Spatial coherence structure and attenuation of the *Lg* phase, site effects, and the interpretation of the *Lg* coda, *Bull. Seism. Soc. Am.*, **74**, 1125-1147.

Fehler, M., Hoshiba, M., Sato, H., & Obara, K., 1992. Separation of scattering and intrinsic attenuation for the Kanto-Tokai region, Japan, using measurements of S-wave energy versus hypocentral distance, *Geophys. J. Int.*, **108**, 787-800.

Frankel, A. & Clayton, R.W., 1986. Finite difference simulations of seismic scattering: implications for the propagation of short-period seismic waves in the crust and models of crustal heterogeneity, *J. Geophys. Res.*, **91**, 6465-6489.

Frankel, A. & Wennerberg, L., 1987. Energy-flux model of seismic data: separation of scattering and intrinsic attenuation, *Bull. Seism. Soc. Am.*, **77**, 1223-1251.

Gupta, I.N., Lynnes, C.S., McElfresh, T.W., & Wagner, R.A., 1990. F-K analysis of Noress array and single station data to indentify sources of near-receiver and near-source scattering, *Bull. Seism. Soc. Am.*, **80**, 2227-2241.

Hedlin, M.A.H., Shearer, P.M., & Earle, P.S., 1997. Seismic evidence for small-scale heterogeneity throughout the Earth's mantle, *Nature*, **387**, 145-150.

Herraiz, M. & Espinosa, A.F., 1987. Coda waves: A review, *Pure Appl. Geophys.*, **125**, 499-577.

Hong, T.-K., 2004. Scattering attenuation ratios of *P* and *S* waves in elastic media, *Geophys. J. Int.*, **158**, 211-224.

Hong, T.-K., & Kennett, B.L.N., 2003. Scattering attenuation of 2-D elastic waves: theory and numerical modelling using a wavelet-based method, *Bull. Seism. Soc. Am.*, **93**, 922-938.

Hong, T.-K., Wu, R.-S. , & Kennett, B.L.N., 2005. Stochastic features of scattering, *Phys. Earth Planet. Inter.*, **148**, 131-148.

Hong, T.-K. & Xie, J., 2005. Phase composition of regional seismic waves from underground nuclear explosions, *J. Geophys. Res.*, **110**, B12302, doi:10.1029/2005JB003753.

Hoshiba, M., 1993. Separation of scattering attenuation and intrinsic absorption in japan using the multiple lapse time window analysis of full seismogram envelope, *J. Geophys. Res.*, **98**, 15,809-15,824.

Hoshiba, M., Rietbrock, A.. Scherbaum, F., Nakahara, H., & Haberland, C., 2001. Scattering attenuation and intrinsic absorption using uniform and depth dependent model - Application to full seismogram envelope recorded in Northern Chile, *J. Seism.*, **5**, 157-179.

Jemberie, A.L. & Langston, C.A., 2005. Site amplification, scattering, and intrinsic attenuation in the Mississippi embayment from coda waves, *Bull. Seism. Soc. Am.*, **95**, 1716-1730.

Jin, A. & Aki, K., 1988. Spatial and temporal correlation between coda Q and seismicity in China, *Bull. Seism. Soc. Am.*, **78**, 741-769.

Kanasewich, E.R., 1981. *Time Sequence Analysis in Geophysics*, Third Edition, The University of Alberta Press, Alberta, Canada.

Kennett, B.L.N., 1986. *Lg* waves and structural boundaries, *Bull. Seism. Soc. Am.*, **76**, 1133-1141.

Kennett, B.L.N., 2001. *The Seismic Wavefield*, volume I: Introduction and Theoretical Development, Cambridge University Press, NY, USA.

Kennett, B.L.N., 2002. *The Seismic Wavefield*, Volume II, Interpretation of Seismograms on Regional and Global Scales, Cambridge University Press, New York.

Kim, W.-Y., Richards, P.G., Adushkin, V., & Ovtchinnikov, V., 2001. Borovoye digital seismogram archive for underground nuclear tests during 1966-1996, Technical Report, Lamont-Doherty Earth Observatory of Columbia University.

Krüger, F., Baumann, M., Scherbaum, F., & Weber, M., 2001. Mid mantle scatterers near the Mariana slab detected with a double array method, *Geophys. Res. Lett.*, **28**, 667-670.

Laske G. & Masters, G., 1997. A global digital map of sediment thickness, *EOS Trans. AGU*, **78**, F483.

La Rocca, M., Del Pezzo, E., Simini, M., Scarpa, R., & De Luca, G., 2001. Array analysis of seismograms from explosive sources: Evidence for surface waves scattered at the main topographical features, *Bull. Seism. Soc. Am.*, **91**, 219-231.

Lee, W.S. & Sato, H., 2005. Power-law decay characteristic of coda envelopes revealed from the analysis of regional earthquakes, Eos Trans. AGU, 86 (52), Fall Meet. Suppl., Abstract S51A-0979.

Lee, W.S., Sato, H., & Lee, K., 2003. Estimation of S-wave scattering coefficient in the mantle from envelope characteristics before and after the ScS arrival, *Geophys. Res. Lett.*, **30** (24), 2248, doi:10.1029/2003GL018413.

Levashova, N.M., Degtyarev, K.E., Bazhenov, M.L., Collins, A.Q., & van der Voo, R., 2003. Permian palaeomagnetism of East Kazakstan and the amalgamation of Eurasia, *Geophys. J. Int.*, **152**, 677-687.

Levshin, A.L. & Ritzwoller, M.H., 1995. Characteristics of surface waves generated by events on and near the Chinese nuclear test site, *Geophys. J. Int.*, **123**, 131-148.

Margerin, L., 2005. Introduction to radiative transfer of seismic waves, in *Seismic Data Analysis with Global and Local Arrays*, eds. A. Levander and G Nolet, AGU Monograph Series, (in press).

Matsumoto, S., Obara, K., & Hasegawa, A., 1998. Imaging P-wave scatterer distribution in the focal area of the 1995 M7.2 Hyogo-ken Nanbu (Kobe) earthquake, *Geophys. Res. Lett.*, **25**, 1439-1442.

Matsumoto, S., Obara, K., & Hasegawa, A., 2001. Characteristics of coda envelope for slant-stacked seismogram, *Geophys. Res. Lett.*, **28**, 1111-1114.

Mitchell, B.J., 1981. Regional variation and frequency dependence of Q_β in the crust of the United States, *Bull. Seism. Soc. Am.*, **71**, 1531-1538.

Nikolaev, A.V. & Troitskiy, P.A., 1987. Lithospheric studies based on array analysis of P-coda and microseismics, *Tectonophysics*, **140**, 103-113.

NNCRK, 1999. Technical Report, Proceedings of the Workshop on IMS Location Calibration, contributed by the National Nuclear Centre of the Republic of Kazakhstan, Olso, Jan 1999.

Padhy, S., 2005. A scattering model for seismic attenuation and its global applications, *Phys. Earth Planet. Inter.*, **148**, 1-12.

Pujades, L.G., Ugalde, A., Canas, J.A., Navarro, M., Badal, F.J., & Corchete, V., 1997. Intrinsic and scattering attenuation from observed seismic codas in the Almeria Basin (southeastern Iberian Peninsula), *Geophys. J. Int.*, **129**, 281-291.

Quin, H.R. & Thurber, C.H., 1992. Seismic velocity structure and event relocation in Kazakhstan from secondary *P* phases, *Bull. Seism. Soc. Am.*, **82**, 2494-2510.

Revenaugh, J., 1995. A scattered-wave image of subduction beneath the transverse range, *Science*, **268**, 1888-1892.

Revenaugh, J., 2000. The relation of crustal scattering to seismicity in southern California, *J. Geophys. Res.*, **105**, 25,403-25,422.

Ringdal, F., Marshall, P.D., & Alewine, R.W., 1992. Seismic yield determination of Soviet underground nuclear explosions at the Shagan River test site, *Geophys. J. Int.*, **109**, 65-77.

Rost, S. & Thomas, C., 2002. Array seismology: methods and applications, *Rev. Geophys.*, **40** (3), 1008, doi:10.1029/2000RG000100.

Sato, H. & Fehler, M., 1998. *Wave propagation and scattering in the heterogeneous Earth*, Springer-Verlag, New York.

Sato, H. & Nishino, M., 2002. Multiple isotropic-scattering model on the spherical Earth for the synthesis of Rayleigh-wave envelopes, *J. Geophys. Res.*, **107** (B12), 2343, doi:10.1029/2001JB000915.

Scherbaum, F., Gillard, D., & Deichmann, N., 1991. Slowness power spectrum analysis of the coda composition of two microearthquake clusters in northern Switzerland, *Phys. Earth Planet. Inter.*, **67**, 137-161.

Scherbaum, F., Krüger, F., & Weber, M., 1997. Double beam imaging: Mapping lower mantle heterogeneities using combinations of source and receiver arrays, *J. Geophys. Res.*, **102**, 507-522.

Shapiro, N.M. & Campillo, M., 2004. Emergence of broadband Rayleigh waves from correlations of the ambient seismic noise, *Geophys. Res. Lett.*, **31**, L07614, doi:10.1029/2004GL019491.

Shapiro, N.M., Campillo, M., Margerin, L., Singh, S.K., Kostoglodov, V., & Pacheco, J., 2000. The energy partitioning and the diffusive character of the seismic coda. *Bull. Seism. Soc. Am.*, 90, 655-665.

Shiomi, K., Sato, H., & Ohtake, M., 1997. Broadband power-law spectra of well-log data in Japan, *Geophys. J. Int.*, **130**, 57-64.

Snieder, R., 1986. The influence of topography on the propagation and scattering of surface waves, *Phys. Earth Planet. Inter.*, **44**, 226-241.

Snieder, R., 1988. Large-scale waveform inversions of surface waves for lateral heterogeneity, 1. Theory and numerical examples, *J. Geophys. Res.*, **93**, 12,055-12,065.

Snieder, R., 2002. Scattering of surface waves, in *Scattering and Inverse Scattering in Pure and Applied Science*, Eds. Pike, R. & P. Sabatier, Academic Press, San Diego, 562-577.

Snieder, R., 2004. Extracting the Green's function from the correlation of coda waves: A derivation based on stationary phase, *Phys. Rev. E.*, **69**, doi:10.1103/PhysRevE.69.046610.

Spudich, P. & Bostwick, T., 1987. Studies of the seismic coda using an earthquake cluster as a deeply buried seismograph array, *J. Geophys. Res.*, **92**, 10,526-10,546.

Taira, T. & Yomogida, K., 2004. Imaging of three-dimensional small-scale heterogeneities in the Hidaka, Japan region: coda spectral analysis, *Geophys. J. Int.*, **158**, 998-1008.

Thurber, C., Trabant, C., Haslinger, F., & Hartog, R., 2001. Nuclear explosion locations at the Balapan, Kazakhstan, nuclear test site: the effects of high-precision arrival times and three-dimensional structure, *Phys. Earth Planet. Inter.*, **123**, 283-301.

Toksöz, MN, Dainty, A.M., Reiter, E.R., & Wu, R.S., 1988, A model for attenuation and scattering in the earth's crust, *Pure Appl. Geophys.*, **128**, 81-100.

Tselentis, G., 1998. Intrinsic and scattering seismic attenuation in W. Greece, *Pure Appl. Geophys.*, **153**, 703-712.

Tusa, G., Malone, S.D., Giampiccolo, E., Gresta, S., & Musumeci, C., 2004. Attenuation of Short-Period P Waves at Mount St. Helens, *Bull. Seism. Soc. Am.*, **94**, 1441-1455.

VanDecar, J.C. & Crosson, R.S., 1990. Determination of teleseismic relative phase arrival times using multi-channel cross correlation and least squares, *Bull. Seism. Soc. Am.*, **80**, 150-169.

Vargas, C.A., Ugalde, A., Pujades, L.G., & Canas, J.A., 2004. Spatial variation of coda wave attenuation in northwestern Colombia, *Geophys. J. Int.*, **158**, 609-624.

Vidale, J.E. & Hedlin, M.A.H., 1998. Evidence for partial melt at the core-mantle boundary north of Tonga from the strong scattering of seismic waves, *Nature*, **391**, 682-685.

Waldhauser, F. & Ellsworth, W.L., 2000. A double-difference earthquake location algorithm: method and application to the northern Hayward fault, California, *Bull. Seism. Soc. Am.*, **90**, 1353-1368.

Wiggins-Grandison, M.D., & Havskov, J., 2004. Crustal attenuation for Jamaica, West Indies, *J. Seismology*, **8**, 193-209.

Wu, R.S., 1982. Attenuation of short period seismic waves due to scattering, *Geophys. Res. Lett.*, **9**, 9-12.

Xie, J., Cong, L., Mitchell, B.J., & Chiu, J.M., 1996. Complexities in high-frequency seismic waveforms due to three-dimensional structure in the New Madrid Seismic Zone, *J. Geophys. Res.*, **101**, 5751-5778.

Xie, J. & Mitchell, B.J., 1990. A back-projection method for imaging large-scale lateral variations of *Lg* coda *Q* with application to continental Africa, *Geophys. J. Int.*, **100**, 161-181.

Yoshimoto, K., 2000. Monte Carlo simulation of seismogram envelopes in scattering media, *J. Geophys. Res.*, **105**, 6153-6161.

Yoshimoto, K., Sato, H., Iio, Y., Ito, H., Ohminato, T., & Ohtake, M., 1998. Frequency-dependent attenuation of high-frequency *P* and *S* waves in the upper crust in western Nagano, Japan, *Pure Appl. Geophys.*, **153**, 489-502.

Zhang, T & Lay, T., 1994. Analysis of short-period regional phase path effects associated with topography in Eurassia, *Bull. Seism. Soc. Am.*, **84**, 119-132.

APPENDIX A: ENSEMBLE-AVERAGED AMPLITUDE SQUARES IN RANDOM MEDIA

Regional phases exhibit a strong impetus of lateral propagation in the crust and lithosphere. The scattering of such regional phases can be well represented with a 2-D model (Jemberie & Langston, 2005). The ensemble-averaged amplitude squares in 2-D random media for *P*-wave incidence are given by (Hong & Kennett, 2003),

$$\begin{aligned}
\langle|u^{PP}|^2\rangle &= \frac{k_\alpha^3\,\mathsf{S}}{8\pi l}[C^{PP}(\phi)]^2\,\mathcal{P}\left[2k_\alpha\,\sin\frac{\phi}{2}\right],\\
\langle|u^{PS}|^2\rangle &= \frac{k_\alpha^3\gamma^3\,\mathsf{S}}{8\pi l}[C^{PS}(\phi)]^2\,\mathcal{P}\left[k_\alpha\sqrt{1+\gamma^2-2\gamma\cos\phi}\right].
\end{aligned} \tag{A.1}$$

and for *S*-wave incidence (Hong, 2004),

$$\begin{aligned}
\langle|u^{SP}|^2\rangle &= \frac{k_\alpha^3\,\mathsf{S}}{\gamma^2 8\pi l}[C^{SP}(\phi)]^2\,\mathcal{P}\left[k_\alpha\sqrt{1+\gamma^2-2\gamma\cos\phi}\right],\\
\langle|u^{SS}|^2\rangle &= \frac{k_\beta^3\,\mathsf{S}}{8\pi l}[C^{SS}(\phi)]^2\,\mathcal{P}\left[2k_\beta\sin\frac{\phi}{2}\right],
\end{aligned} \tag{A.2}$$

where k_α and k_β are the wavenumbers of *P* and *S* waves, γ is the ratio of background *P* and *S* wave velocities (α_0/β_0), S is the surface area of heterogeneity, l is the propagation distance, ϕ is the scattering angle, and $\mathcal{P}$ is the spectral density function of the random medium. The coefficient C^{ij} ($i,j=P,S$) is given by

$$\begin{aligned}
C^{PP}(\phi) &= \sin\phi\left\{C_1^P A_{11}^P(\phi)\sin\phi + 2A_{12}^P(\phi) + C_2^P A_{12}^P(\phi)(\cos\phi-1)\right\}\\
&\quad+\cos\phi\left\{C_1^P A_{21}^P(\phi)\sin\phi + 2A_{22}^P(\phi) + C_2^P A_{22}^P(\phi)(\cos\phi-1)\right\},\\
C^{PS}(\phi) &= \cos\phi\left\{C_1^P A_{11}^S(\phi)\gamma\sin\phi + 2A_{12}^S(\phi) + C_2^P A_{12}^S(\phi)(\gamma\cos\phi-1)\right\}\\
&\quad-\sin\phi\left\{C_1^P A_{21}^S(\phi)\gamma\sin\phi + 2A_{22}^S(\phi) + C_2^P A_{22}^S(\phi)(\gamma\cos\phi-1)\right\},\\
C^{SP}(\phi) &= \sin\phi\left\{-\gamma C_1^S A_{11}^P(\phi) + (\cos\phi-\gamma)C_2^S A_{11}^P(\phi) + \sin\phi\, C_2^S A_{12}^P(\phi)\right\}\\
&\quad+\cos\phi\left\{-\gamma C_1^S A_{21}^P(\phi) + (\cos\phi-\gamma)C_2^S A_{21}^P(\phi) + \sin\phi\, C_2^S A_{22}^P(\phi)\right\},\\
C^{SS}(\phi) &= \cos\phi\left\{-C_1^S A_{11}^S(\phi) + (\cos\phi-1)C_2^S A_{11}^S(\phi) + \sin\phi\, C_2^S A_{12}^S(\phi)\right\}\\
&\quad-\sin\phi\left\{-C_1^S A_{21}^S(\phi) + (\cos\phi-1)C_2^S A_{21}^S(\phi) + \sin\phi\, C_2^S A_{22}^S(\phi)\right\},
\end{aligned} \tag{A.3}$$

where C_i^j ($i=1,2$, $j=P,S$) is

$$C_1^P = (K+2)\left(1-\frac{2}{\gamma^2}\right),\quad C_2^P = K+2,\quad C_1^S = -2,\quad C_2^S = K+2, \tag{A.4}$$

and K is the constant in (1). Also, A_{ij}^k (i,j=1,2, k=P,S) is given by

$$\begin{aligned}
&A_{11}^P(\phi)=\sin^2\phi,\quad A_{12}^P(\phi)=\sin\phi\cos\phi,\quad A_{21}^P(\phi)=-\sin\phi\cos\phi,\quad A_{22}^P(\phi)=\cos^2\phi,\\
&A_{11}^S(\phi)=\cos^2\phi,\quad A_{12}^S(\phi)=-\sin\phi\cos\phi,\quad A_{21}^S(\phi)=\sin\phi\cos\phi,\quad A_{22}^S(\phi)=\sin^2\phi.
\end{aligned} \tag{A.5}$$

Figure 1. Energy ratios, R, between in-phase and wavetype-coupled scattered waves in elastic random media (von Karman, exponential, Gaussian). (a) Scattered energy ratios for *P*-wave incidence case (R =[*PS* energy]/[*PP* energy]) and (b) for *S*-wave incidence case (R =[*SP* energy]/[*SS* energy]). In the *P*-wave incidence, the wavetype-coupled scattered waves are stronger than in-phase scattered waves at lower normalized wavenumbers, $ka < 2$. In-phase scattered waves are dominant over wavetype-coupled scattered waves in the entire ka range for the *S*-wave incidence case.

Figure 2. Schematic diagram of locationing of a heterogeneity using traveltime, beamforming direction and phase velocity. Source-array beams which are radiated into an azimuthal direction of θ are back-scattered by a heterogeneity, and the scattered waves are recorded at a receiver. The locations of events and receiver are the foci of iso-travel distance ellipses. The size of iso-travel ellipse is determined by the traveltime and phase velocity. Coherent scattered waves with a common phase velocity can be assessed by slant-stacking the source-array records for an azimuthal angle of θ.

Figure 3. Schematic diagram of source-array beamforming for an azimuthal angle of θ_j. The source array (clustered events) is marked with solid circles, and an imaginary reference location for beamforming direction is marked with an inverted triangle. The reference location of the source array is $\mathbf{x}_0$, the location of ith event is $\mathbf{x}_i$, and the location of the imaginary receiver is $\mathbf{y}_j$. The distance between $\mathbf{y}_j$ and $\mathbf{x}_0$ is r_0 which is constant for a change in azimuthal angle. The distance between $\mathbf{y}_j$ and $\mathbf{x}_i$ is r_i^j.

Figure 4. An example of slant-stackings in a four-component array for two different beamforming directions, θ_1 and θ_2. The distance between array and imaginary reference location changes with a beamforming direction, which causes a change in the order of records for distance. The shaded areas indicate the wavelets with a given phase velocity.

Figure 5. (a) 46 low-gain and (b) 35 high-gain seismograms, which are arranged for epicentral distances. The coda amplitudes of low-gain seismograms are very low at long lapse times, and are subject to digitizing roundoff error. The high-gain records are used for an analysis of lapse times after 400 s.

Figure 6. (a) Underground nuclear explosions in Balapan test site, Kazakhstan, which are used in this study. The numbers of events recorded at low-gain and high-gain seismometers are 46 and 35, respectively. Most events were recorded at both low- and high-gain seismometers. (b) Vertical variation of events relative to the reference location of 49.92°N and 78.82°E, and 155 m below the sea level, in a view on the longitudinal direction. The vertical deviation from the average depth varies up to 300 m. The source-array aperture is about 19 km in the longitudinal direction.

Figure 7. (a) Crustal thickness (CRUST2.0), (b) sedimentary thickness, (c) surface topography (GTOPO30), and (d) major geological structures (modified after Levashova *et al.* (2003)) in central Asia. Iso-travel distances are marked with lines in every 500 km. The locations of receiver and source array correspond to the foci of iso-travel distance ellipses.

Figure 8. Array response functions of the source array for various frequency bands: (a) 0.2-0.4 Hz, (b) 0.4-0.8 Hz, (c) 0.8-1.6 Hz and (d) 1.6-3.2 Hz. The energy is concentrated in the centers of slowness power spectrum diagrams, which indicates a high-resolving power of F-K analysis without any noticeable aliasing effects.

Figure 9. Slowness power spectra of seismic coda with bandpass filterings. The bandpass filtering ranges are (a) 0.2-0.4 Hz, (b) 0.4-0.8 Hz, (c) 0.8-1.6 Hz, and (d) 1.6-3.2 Hz. *pmax* indicates the normalized maximum power ($0 \leq pmax \leq 1$). Strong coherent energy is observed in low-frequency regimes of 0.2-0.4 Hz and 0.4-0.8 Hz, while high-frequency energy appears to be diffused (0.8-1.6 Hz, 1.6-3.2 Hz). The coherent energy in the low-frequency regimes is observed consistently until the ends of records. The phase velocity of this coherent energy is about 3.0 km/s which corresponds to *Rg* phase velocity.

Figure 10. Normalized scattered *Rg* energy variation with azimuthal angle at a lapse time of t. The scattered energy is normalized for the maximum strength. The normalized amplitude indicates the relative strength of constituent scattered energy with azimuthal direction.

Figure 11. Normalized scattered energy variation ((a) *Rg*, (b) *Lg*) with lapse time and azimuthal angle, which is an integration of temporal variation of normalized scattering energy in Fig. 10. The lapse time of record section and the azimuthal angle for slant-stacking are annotated.

Figure 12. Spatial variations of normalized scattering intensities which are measured from (a) *Rg*, (b) *Lg*, (c) *Sn*, and (d) *Pg* scattered waves. Travel-distance lines are presented, and their corresponding lapse times are also annotated. The illuminated scattering locations agree with structural variations in Fig. 7.

Figure 13. Mapping of scattering intensity under *Lg*-to-*Pg* scattering concept. Since the phase velocity of scattered wave is higher than that of incident wave, the locations of heterogeneities are shifted away from the source array the estimated location is estimated to be away from the source array. The illuminated scattering locations appear to be less conforming to the geological variation in Fig. 7 (e.g., high surface topography region at the south of Balapan test around 45°N and 82°E).

Figure 14. Spatial variation of quality factors, Q, estimated from (a) *Rg*, (b) *Lg*, (c) *Sn*, and (d) *Pg* scattered waves. The attenuation of surface waves are stronger than that of body waves. *Rg* phase is strongly attenuated by a variation in surface topography. The influence of surface topography appears to be relatively weak on the attenuation of *Lg* and body waves. Color bars are scaled for clear presentation.

Figure 15. Spatial variation of apparent scattering coefficients, g_0, estimated from (a) *Rg*, (b) *Lg*, (c) *Sn*, and (d) *Pg* scattered waves. The scattering coefficients from *Rg* and *Lg* scattered waves are larger than those from *Sn* and *Pg* scattered waves. Color bars are scaled for clear presentation.

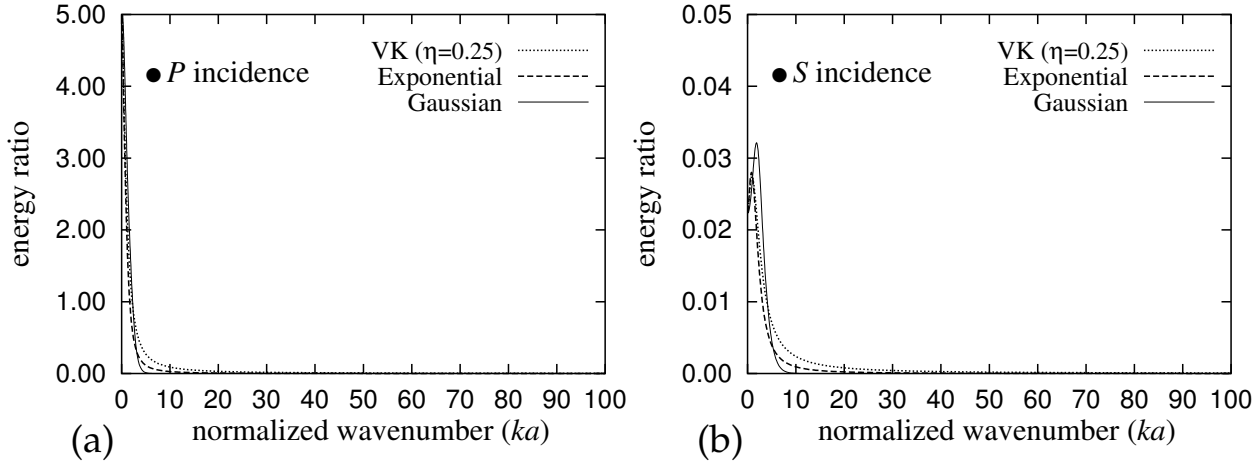
5.00
4.00
3.00
2.00
1.00
0.00
energy ratio
● P incidence
VK (η=0.25)
Exponential
Gaussian
0 10 20 30 40 50 60 70 80 90 100
normalized wavenumber (ka)
(a)
0.05
0.04
0.03
0.02
0.01
0.00
energy ratio
● S incidence
VK (η=0.25)
Exponential
Gaussian
0 10 20 30 40 50 60 70 80 90 100
normalized wavenumber (ka)
(b)

Figure 1

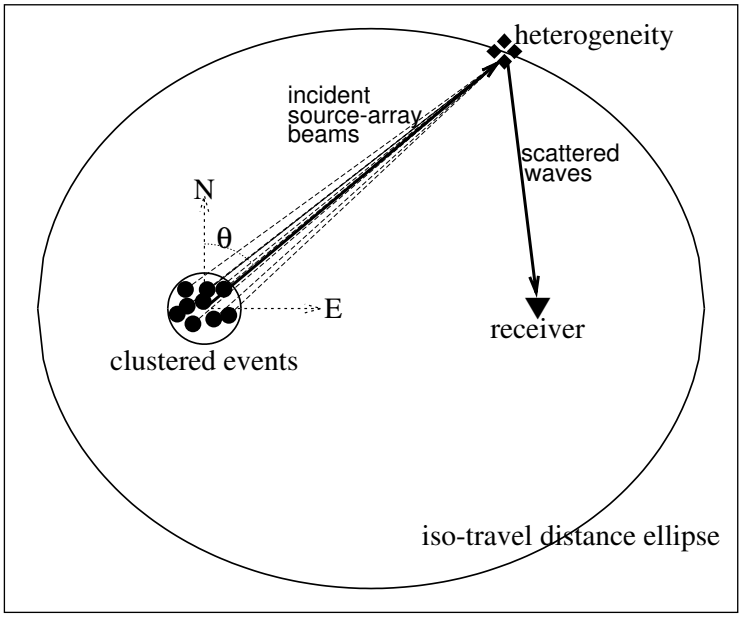
heterogeneity
incident
source-array
beams
scattered
waves
N
θ
E
receiver
clustered events
iso-travel distance ellipse

Figure 2

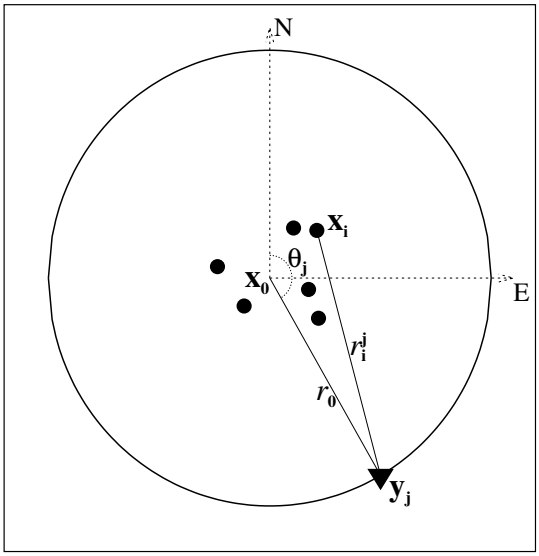

Figure 3

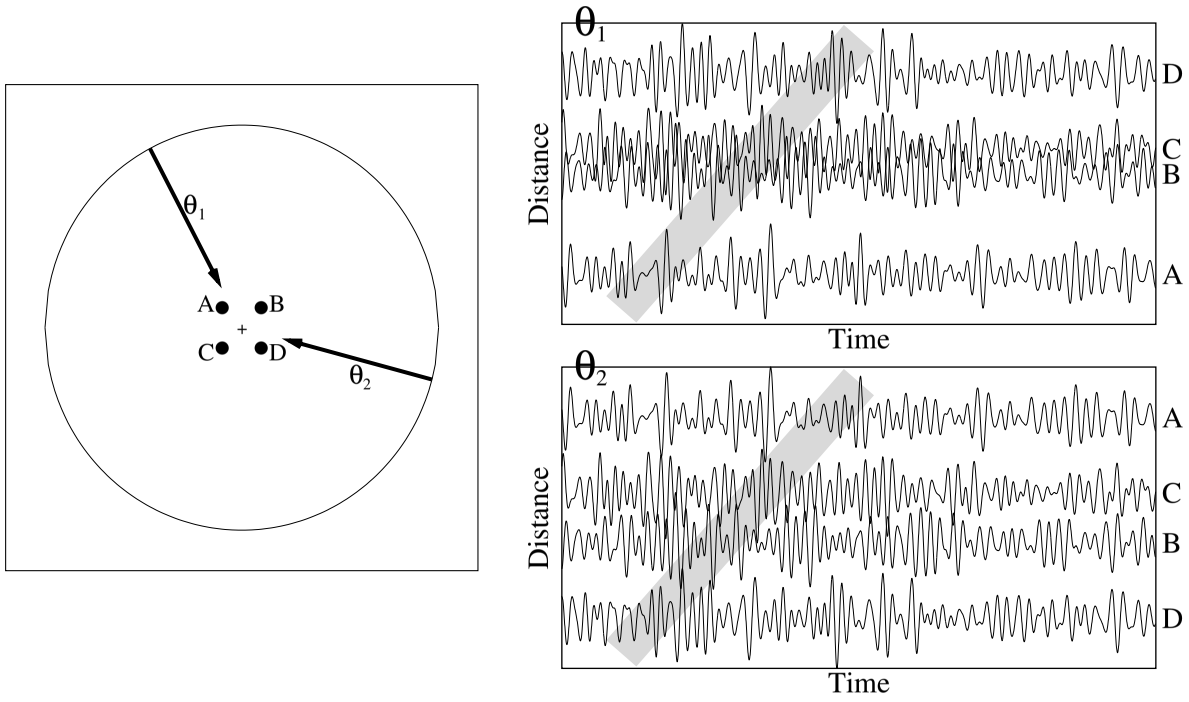

Figure 4

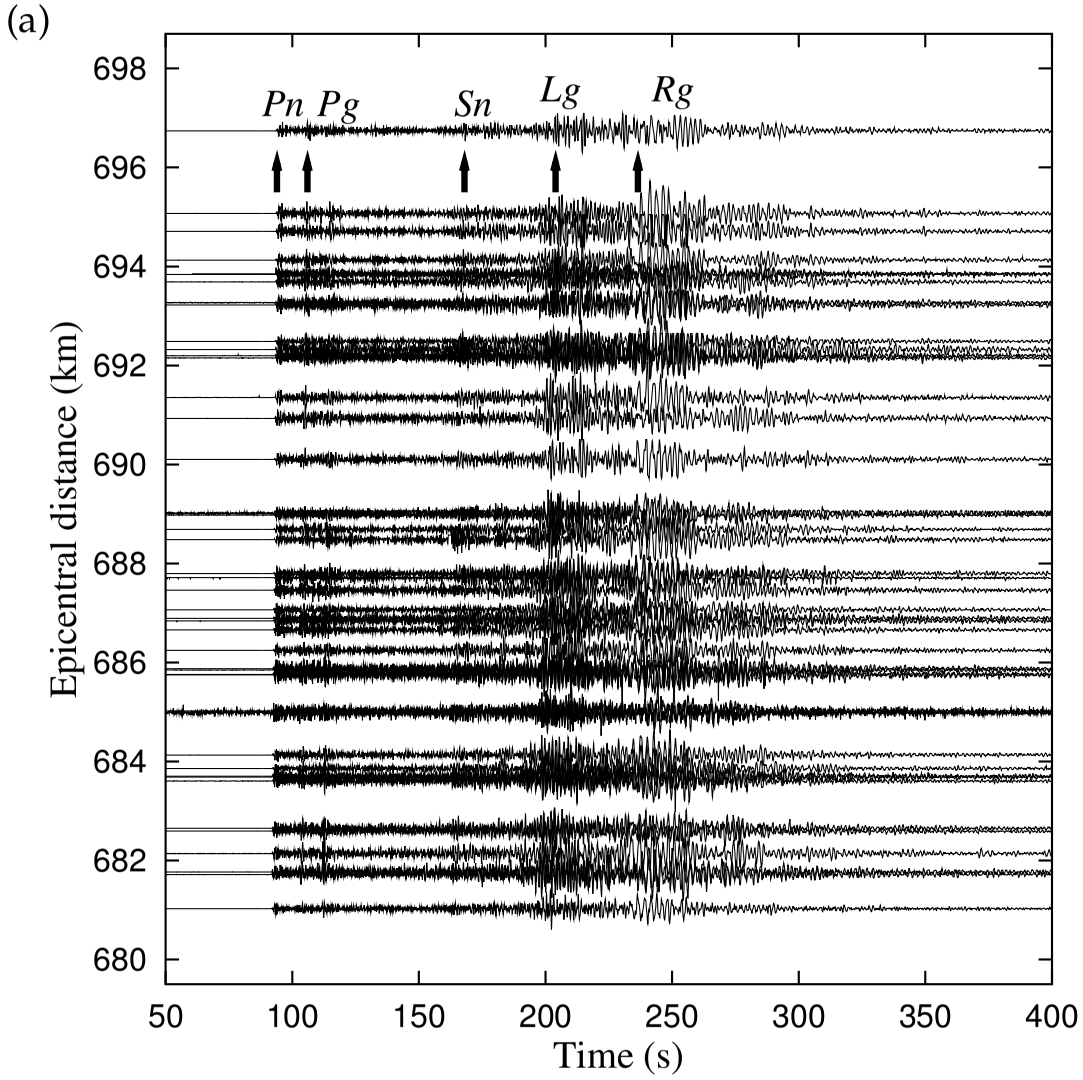
(a)
Pn
Pg
Sn
Lg
Rg
Epicentral distance (km)
698
696
694
692
690
688
686
684
682
680
50
100
150
200
250
300
350
400
Time (s)

Figure 5

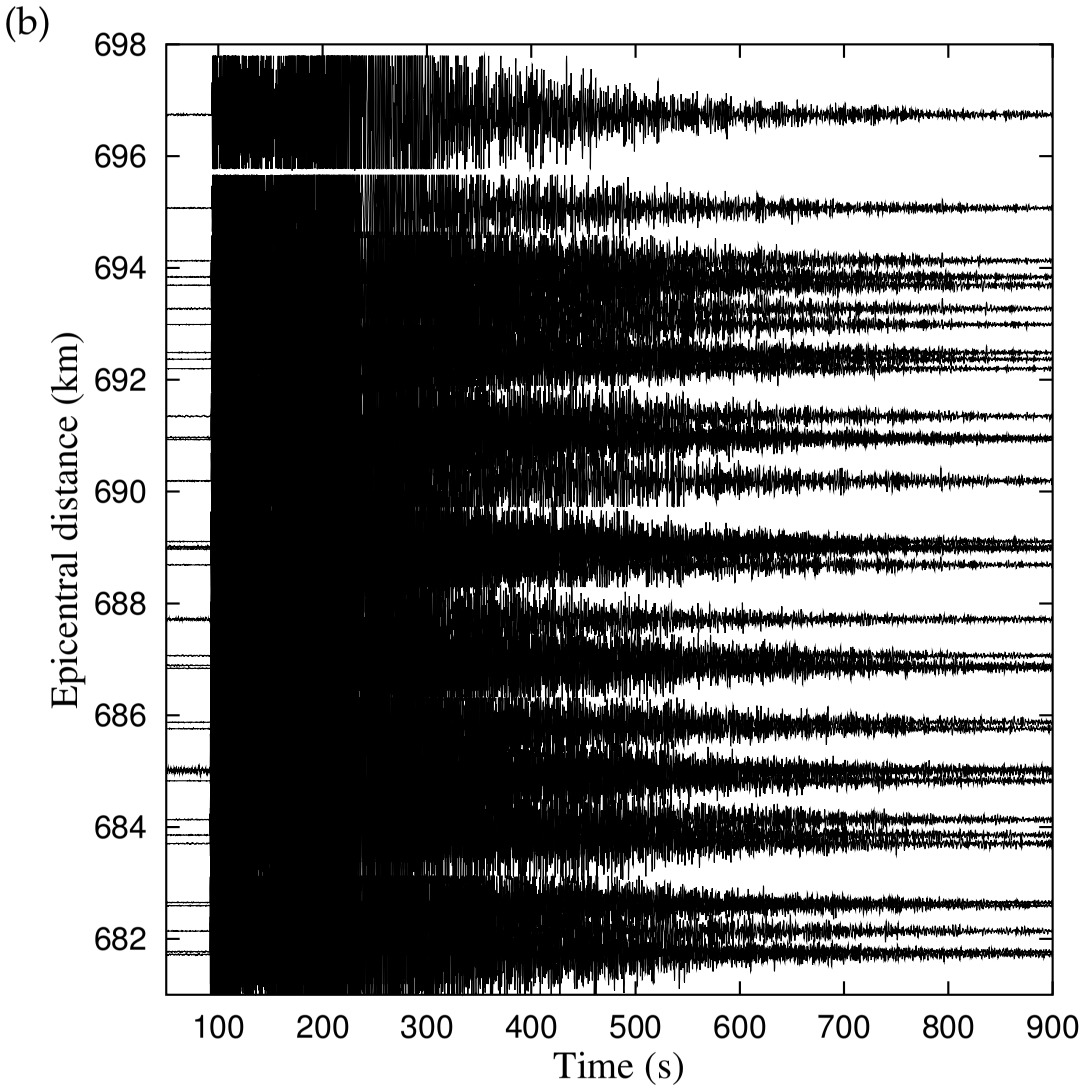

Figure 5 (*continued*)

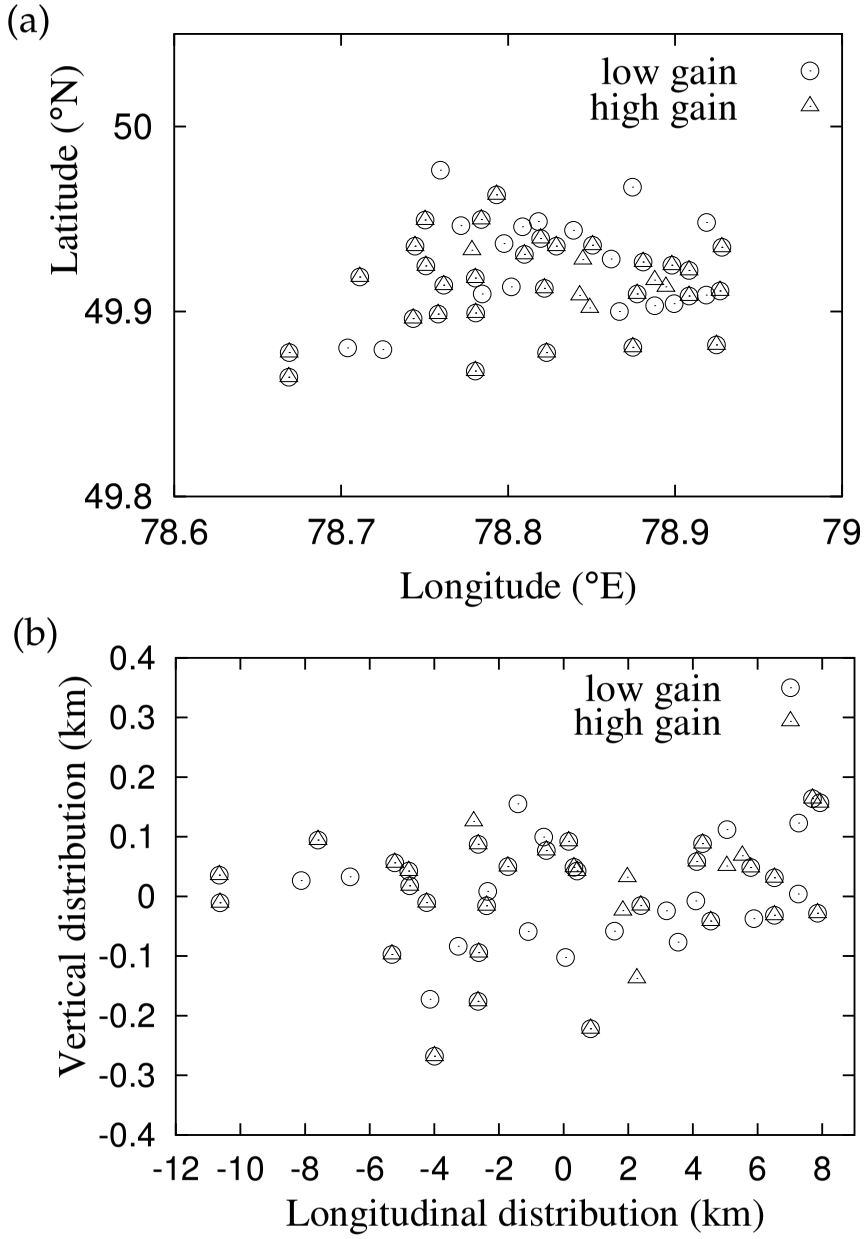
(a)
low gain
high gain
Latitude (°N)
50
49.9
49.8
78.6
78.7
78.8
78.9
79
Longitude (°E)
(b)
low gain
high gain
Vertical distribution (km)
0.4
0.3
0.2
0.1
0
-0.1
-0.2
-0.3
-0.4
-12
-10
-8
-6
-4
-2
0
2
4
6
8
Longitudinal distribution (km)

Figure 6

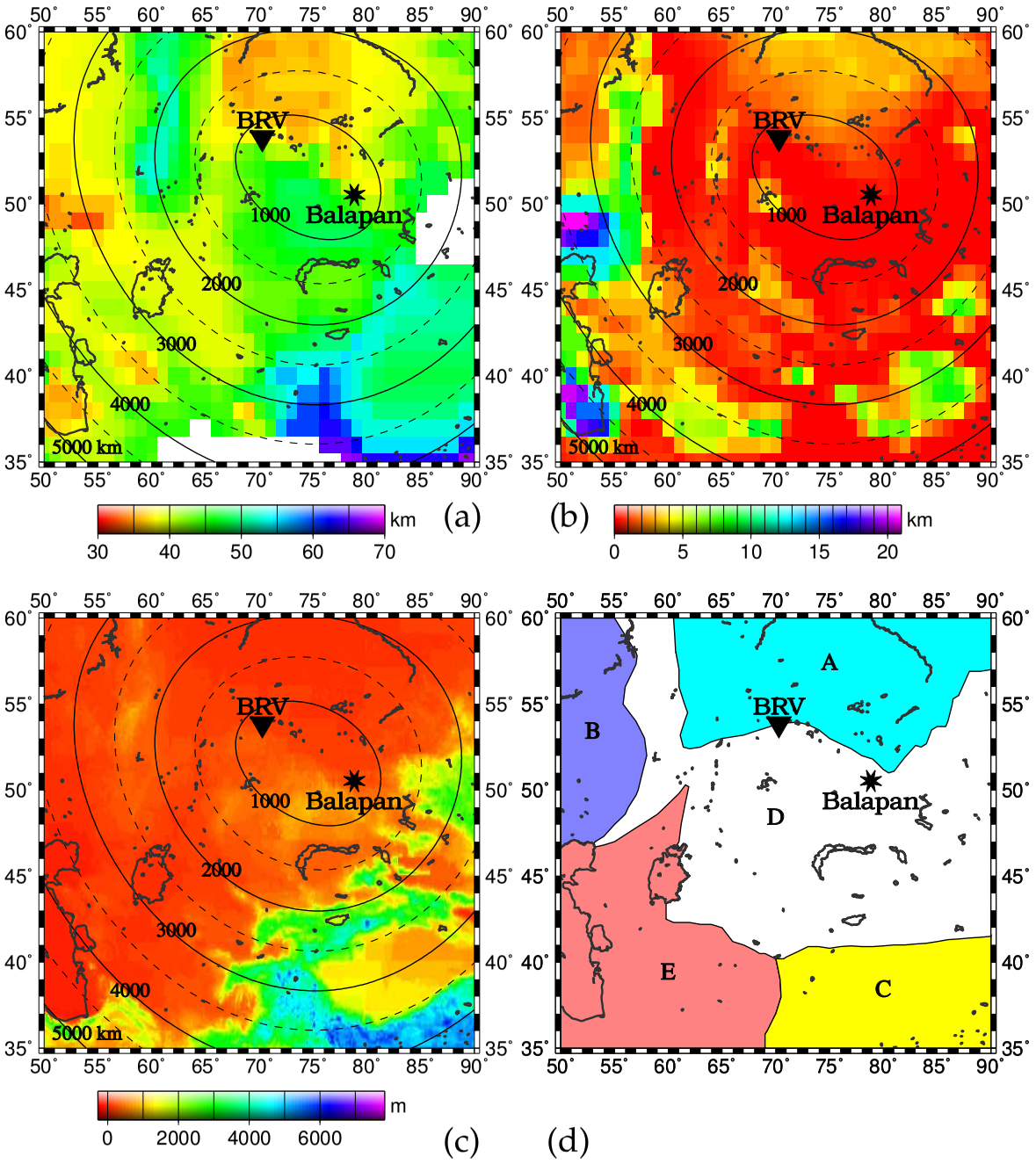
BRV
Balapan
1000
2000
3000
4000
5000 km
km
30 40 50 60 70
(a)
0 5 10 15 20
(b)
m
0 2000 4000 6000
(c)
A
B
C
D
E
(d)

Figure 7

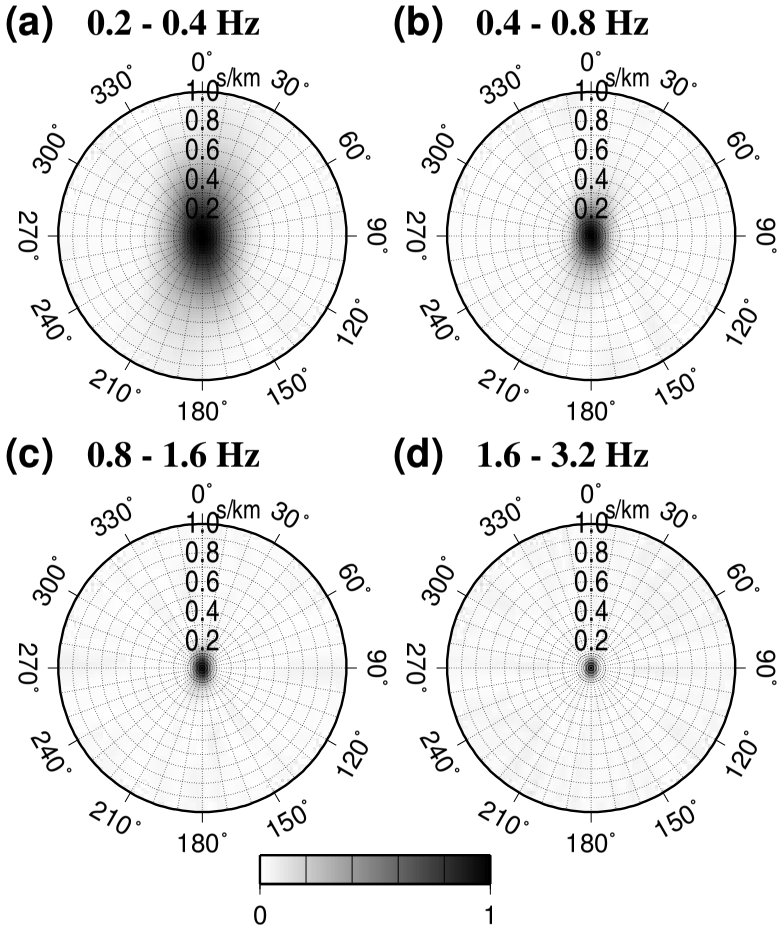
(a) 0.2 - 0.4 Hz
(b) 0.4 - 0.8 Hz
(c) 0.8 - 1.6 Hz
(d) 1.6 - 3.2 Hz
s/km
0.2
0.4
0.6
0.8
1.0
0°
30°
60°
90°
120°
150°
180°
210°
240°
270°
300°
330°
0
1

Figure 8

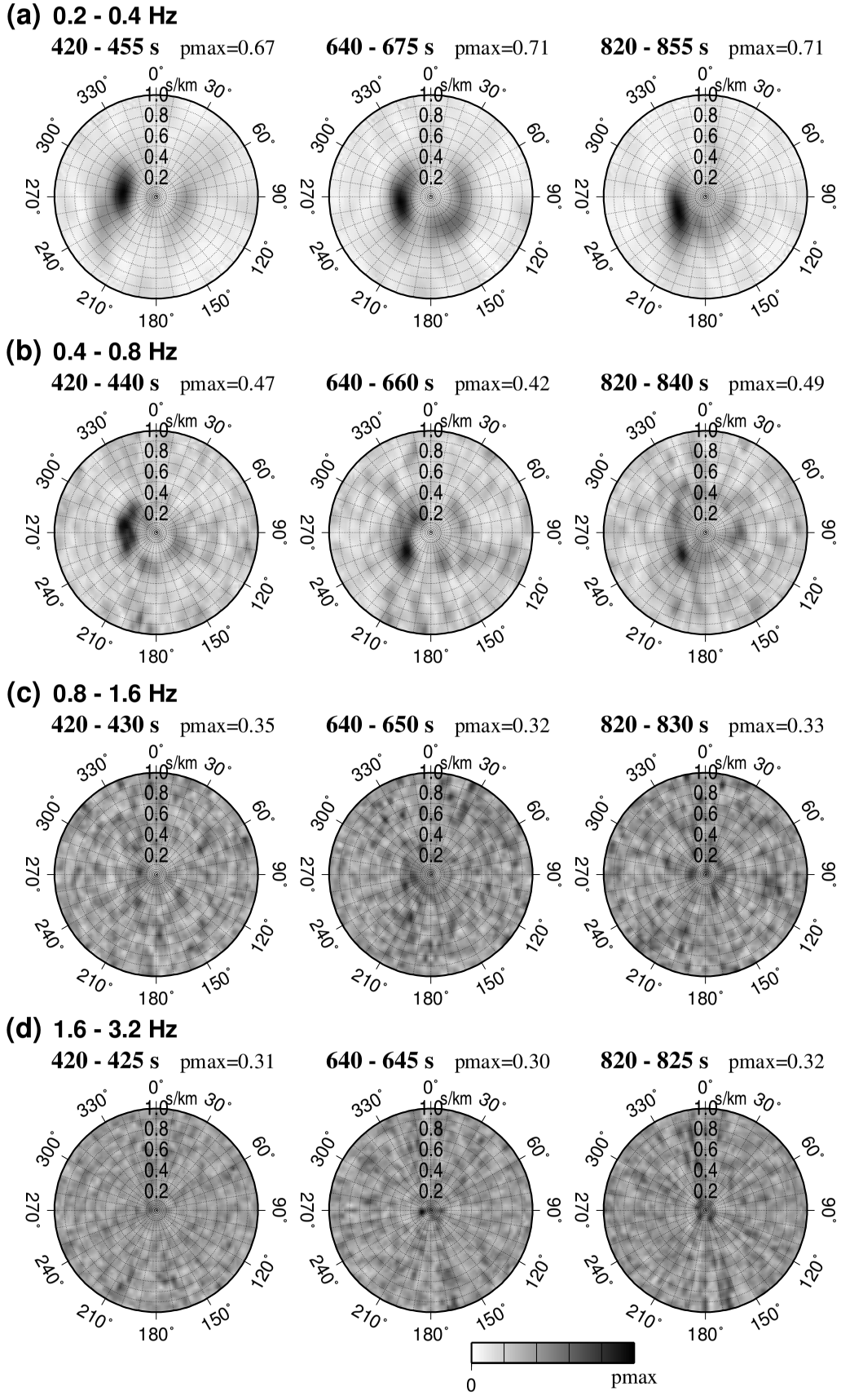
(a) 0.2 - 0.4 Hz
420 - 455 s pmax=0.67
640 - 675 s pmax=0.71
820 - 855 s pmax=0.71
(b) 0.4 - 0.8 Hz
420 - 440 s pmax=0.47
640 - 660 s pmax=0.42
820 - 840 s pmax=0.49
(c) 0.8 - 1.6 Hz
420 - 430 s pmax=0.35
640 - 650 s pmax=0.32
820 - 830 s pmax=0.33
(d) 1.6 - 3.2 Hz
420 - 425 s pmax=0.31
640 - 645 s pmax=0.30
820 - 825 s pmax=0.32
s/km
0
pmax

Figure 9

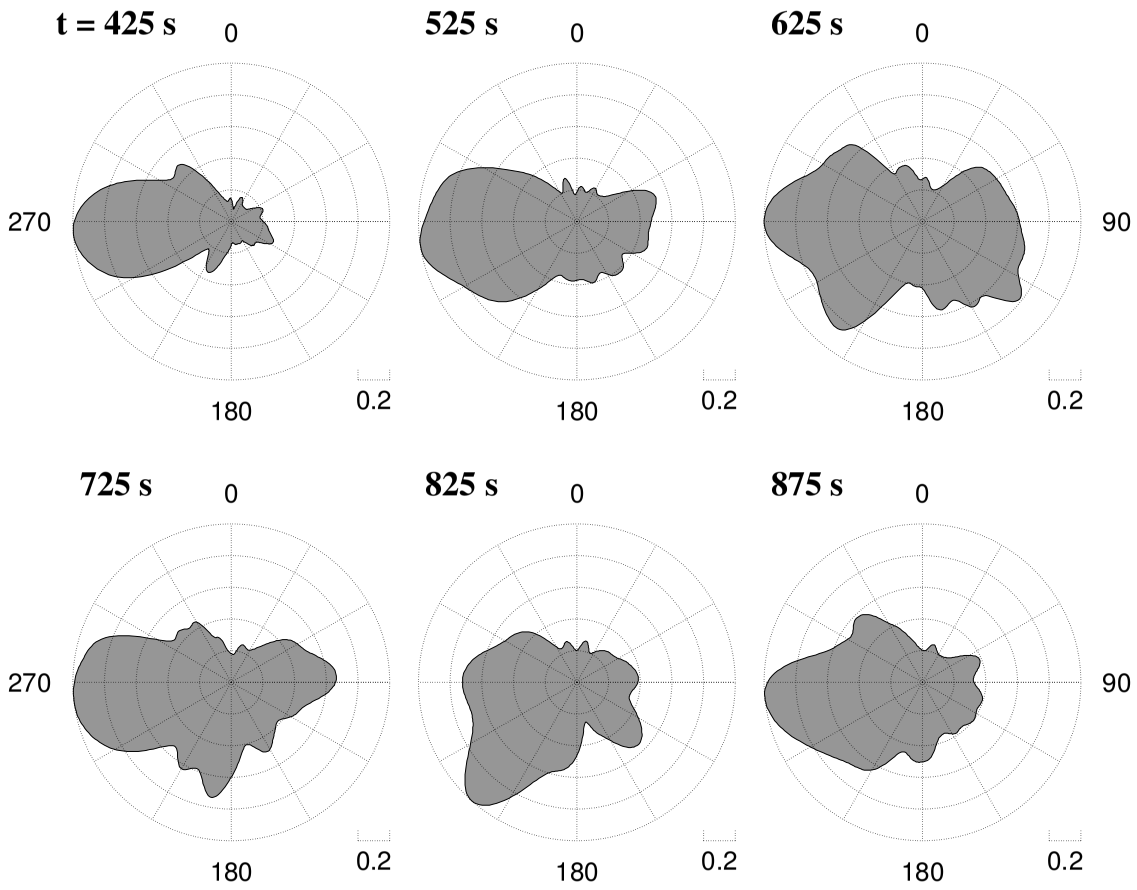

Figure 10

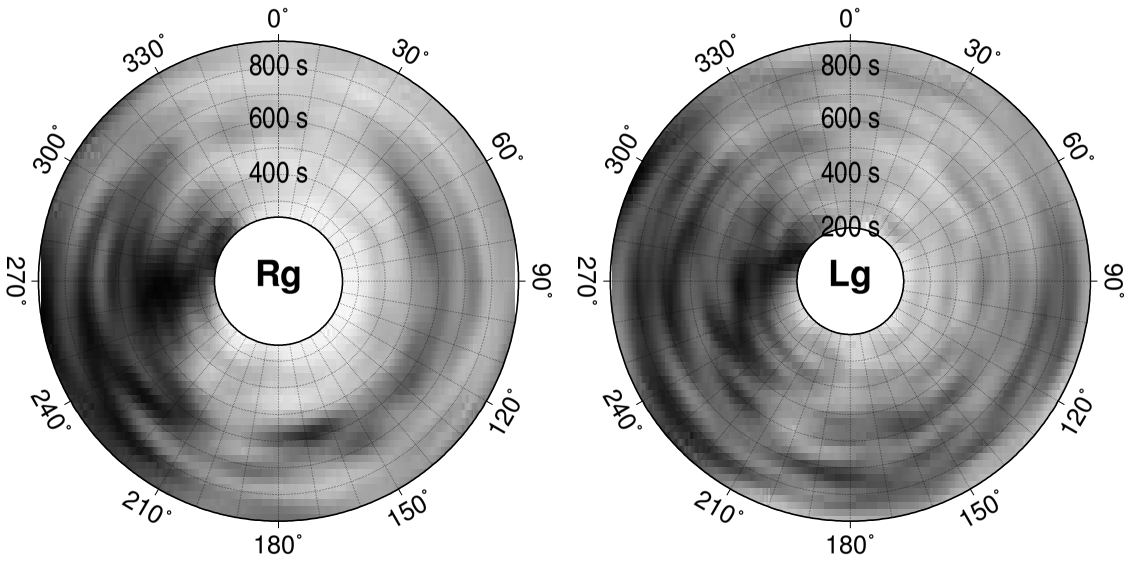
0˚
30˚
60˚
90˚
120˚
150˚
180˚
210˚
240˚
270˚
300˚
330˚
800 s
600 s
400 s
Rg
200 s
Lg

(a) (b)

Figure 11

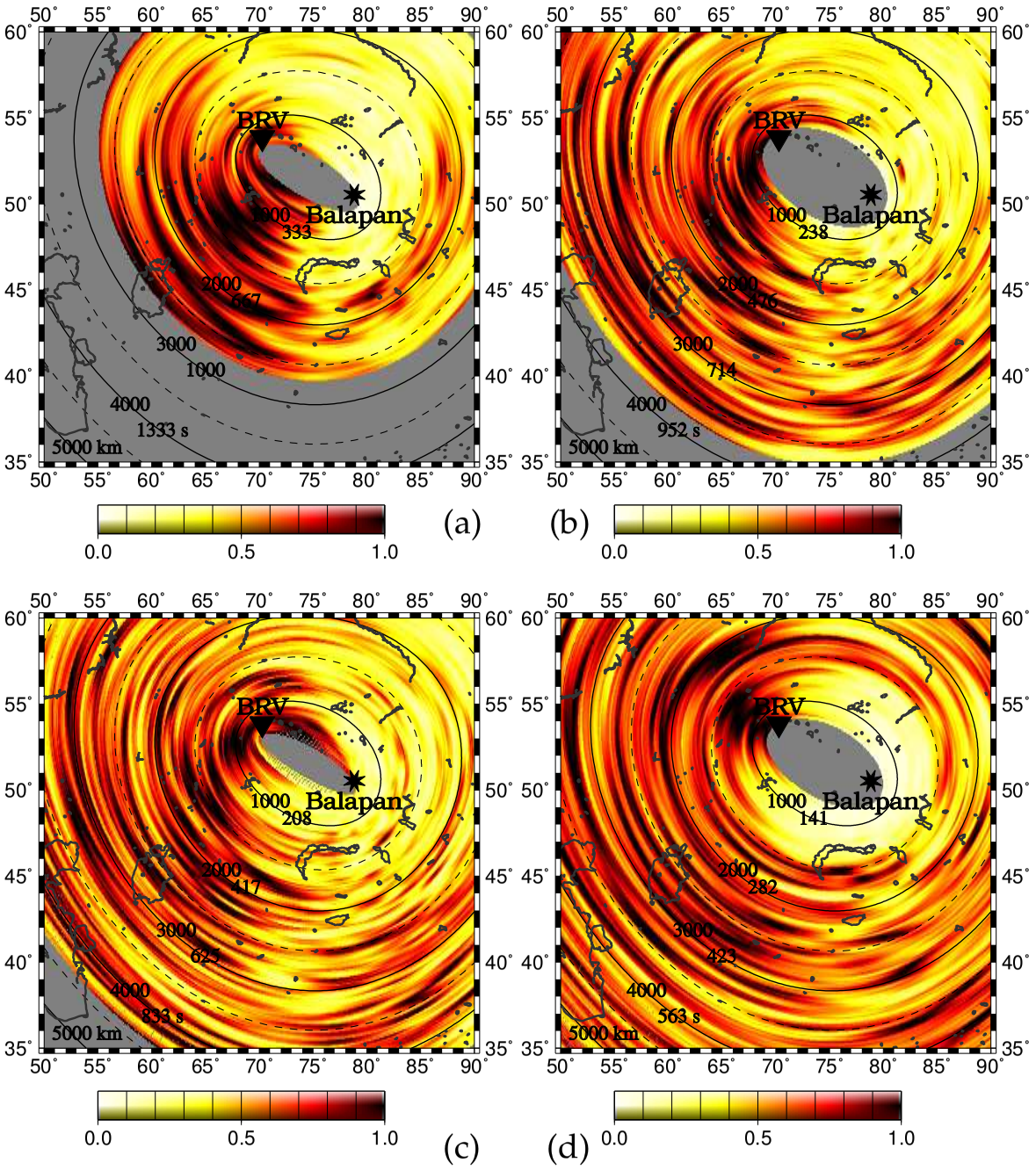
BRV
Balapan
1000
333
2000
667
3000
1000
4000
1333 s
5000 km
(a)
1000
238
2000
476
3000
714
4000
952 s
5000 km
(b)
1000
208
2000
417
3000
625
4000
833 s
5000 km
(c)
1000
141
2000
282
3000
423
4000
563 s
5000 km
(d)
0.0
0.5
1.0

Figure 12

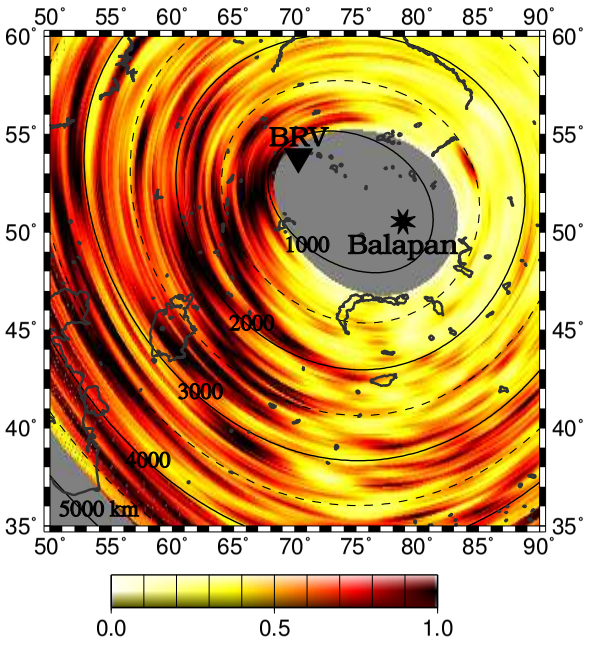
50˚ 55˚ 60˚ 65˚ 70˚ 75˚ 80˚ 85˚ 90˚
60˚
55˚
50˚
45˚
40˚
35˚
BRV
Balapan
1000
2000
3000
4000
5000 km
0.0
0.5
1.0

Figure 13

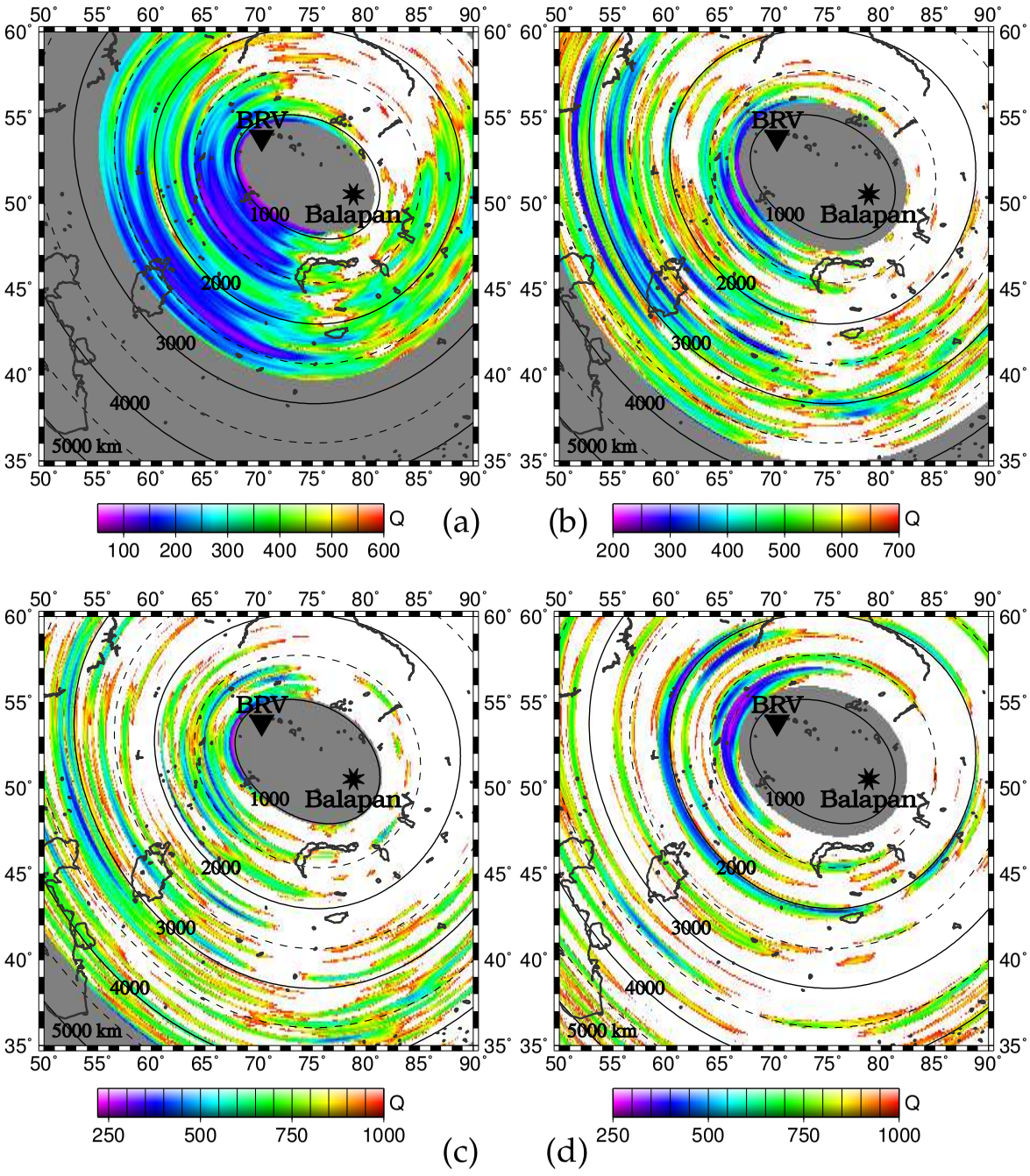
BRV
Balapan
1000
2000
3000
4000
5000 km
Q
100 200 300 400 500 600
(a)
200 300 400 500 600 700
(b)
250 500 750 1000
(c)
(d)

Figure 14

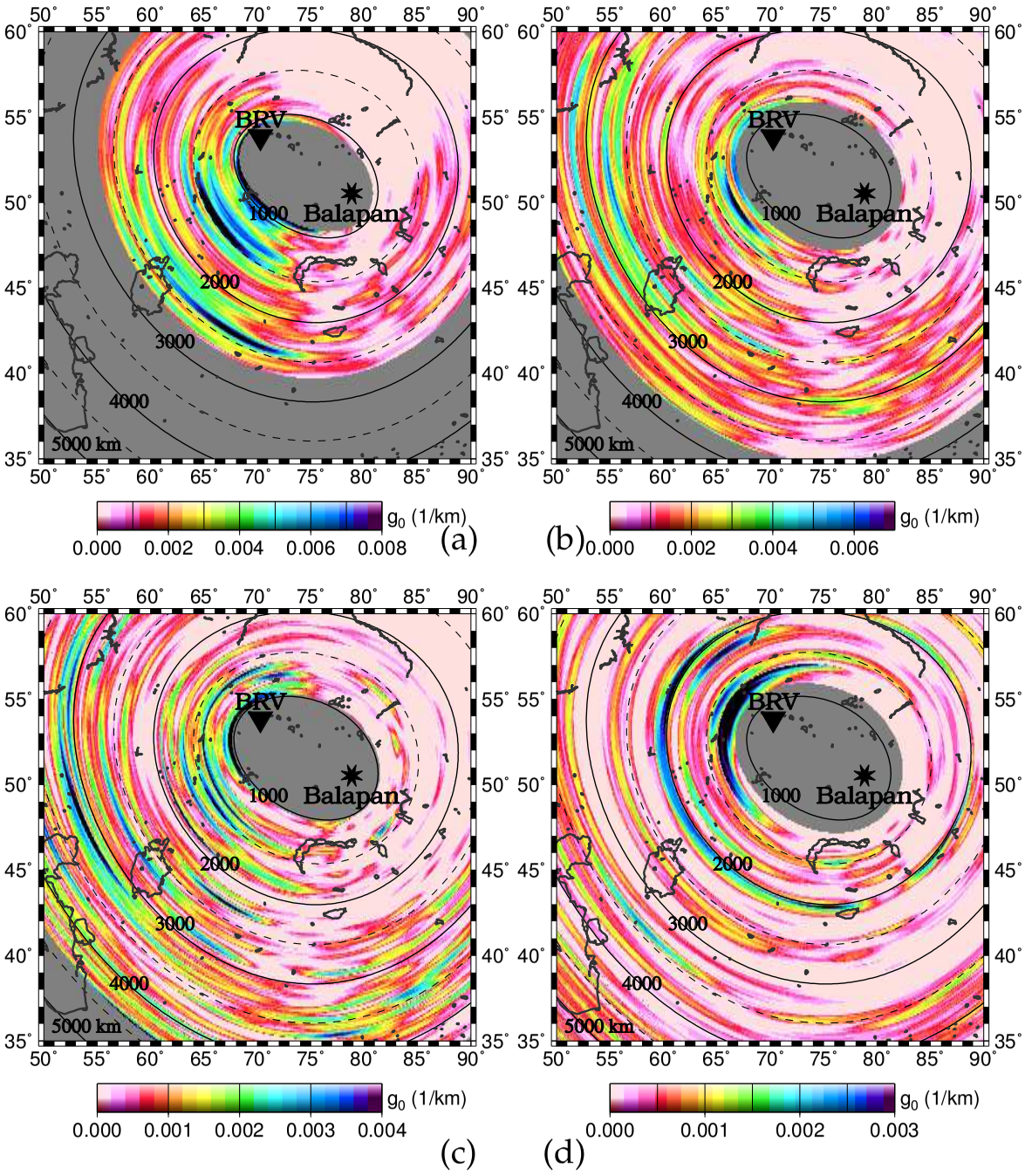
BRV
Balapan
1000
2000
3000
4000
5000 km
g_0 (1/km)
0.000 0.002 0.004 0.006 0.008
(a)
(b)
0.000 0.002 0.004 0.006
0.000 0.001 0.002 0.003 0.004
(c)
(d)
0.000 0.001 0.002 0.003

Figure 15